

The transport and deposition of heavy particles in complex terrain: insights from an Eulerian model for large eddy simulation

S. T. Salesky¹, M. G. Giometto², M. Chamecki³, M. Lehning^{2,4}, and M. B. Parlange⁶

Abstract.

The transport and deposition of heavy particles over complex surface topography by turbulent fluid flow is an important problem in a number of disciplines, including sediment and snow transport, ecology and plant pathology, aeolian processes, and geomorphology. This article presents a framework to simulate the transport and deposition of heavy particles over complex surfaces using the large eddy simulation (LES) technique. An immersed boundary LES code is coupled with an Eulerian particle code that solves the advection-diffusion equation for the resolved particle concentration field. The mass conservation equation for the particle phase is discretized in a finite volume framework using a Cartesian cut cell method that reshapes finite volume cells intersected by the immersed boundary surface and conserves mass accurately. The proposed numerical model is compared with data from wind tunnel experiments of heavy particle deposition over topography and is found to have good agreement with observed deposition patterns. An LES case study of snow deposition over idealized topography leads to several new insights. Particle inertia leads to relative velocities between the particles and fluid in regions of mean flow acceleration, thereby enhancing deposition on the windward side of obstacles and suppressing deposition on the leeward side. In addition, it is found that the mean components of particle inertia are a factor of 6 or more larger than the turbulent components, indicating that the enhancement/suppression of deposition by topography can be modeled in terms of mean flow quantities.

1. Introduction

The transport, erosion, and deposition of heavy particles over complex surface topography due to turbulent flow is an important process for a diverse set of research problems, including alpine hydrology and ecology; avalanche prediction; dune formation and evolution; the dispersal of pollen, seeds, and spores; the emission of mineral dust aerosols; stream bank erosion; and scour around hydraulic structures.

Snow deposition, erosion, and transport over complex topography are important processes in the context of alpine and polar hydrology, ecology, and avalanche prediction. A number of studies have demonstrated that the spatial distribution of snowpack depth and snow water equivalent are closely linked to topography [e.g. *Elder et al.*, 1991; *Blöschl and Kirnbauer*, 1992; *Liston and Sturm*, 1998; *Luce et al.*,

1998; *Balk and Elder*, 2000; *Lehning et al.*, 2008]. Spatial inhomogeneities in snowpack depth have a strong influence on the timing of surface runoff through snowpack melt; *Luce et al.* [1998] found that errors in estimates of snowpack depth led to basin-wide errors in runoff and evapotranspiration in distributed hydrological models. Runoff from snow melt is a major source of nutrients for alpine ecosystems [*Bowman*, 1992; *Walker et al.*, 1993], and snowpack depth can influence the spatial variability of available moisture, which is a determining factor for the spatial distribution of vegetation cover [*Evans et al.*, 1989]. In addition, the inhomogeneous transport and deposition of snow in complex terrain can be a contributing factor for avalanche formation [e.g. *Perla et al.*, 1976; *Schweizer et al.*, 2003]. Snow cornices [*Kobayashi et al.*, 1988; *Vogel et al.*, 2012] frequently form on the leeward side of ridges; cornice failure often triggers avalanche formation. Furthermore, snow transport is a significant process influencing the mass balance of ice sheets [e.g. *Eisen et al.*, 2008; *Scarchilli et al.*, 2010; *Das et al.*, 2013, 2015] and continental glaciers [*Déry et al.*, 2010].

In the context of sediment transport, saltating sand particles can be a source of mineral dust aerosols [*Shao et al.*, 1993], which have important implications for climate, ecology, and hydrology [e.g. *Shao et al.*, 2011; *Kok et al.*, 2012]. Radiative feedbacks due to dust remain a significant source of climate uncertainty [*Sokolik et al.*, 2001]. Aeolian dust transport to the oceans is a significant source of nutrients (e.g. iron) that affect ocean ecology and biogeochemistry [*Jickells et al.*, 2005]. In addition, mineral dust aerosols have complex feedbacks on the hydrological cycle, leading to surface radiative forcings that reduce global precipitation, but increase precipitation in arid regions [*Miller et al.*, 2004].

Interactions between a turbulent flow and mobile sediment bed can lead to the formation of a variety of bedforms

¹School of Meteorology, University of Oklahoma, Norman, OK, USA

²Department of Civil Engineering and Engineering Mechanics, Columbia University, New York, NY, USA

³Department of Atmospheric and Oceanic Sciences, University of California Los Angeles, Los Angeles, CA, USA

⁴School of Architecture, Civil and Environmental Engineering, Swiss Federal Institute of Technology, Lausanne, Switzerland

⁵WSL Institute for Snow and Avalanche Research SLF, Davos, Switzerland

⁶Department of Civil Engineering, Monash University, Clayton, Australia

including ripples and dunes [e.g. *Bagnold*, 1941; *Engelund and Fredsoe*, 1982; *Charru et al.*, 2013]; recent studies have demonstrated how these bedforms can propagate as sand waves [e.g. *Venditti et al.*, 2005; *Khosronejad and Sotiropoulos*, 2014]. The formation and migration of these bedforms in rivers can affect stream ecology [*MacVicar et al.*, 2006] and can cause riverbank erosion during floods [*Best*, 2005; *MacVicar et al.*, 2006]. In addition, the presence of bedforms in rivers can also enhance the exchange of solutes and particles in the hyporheic zone [*Packman and Brooks*, 2001; *Packman et al.*, 2004] which impact contaminant transport and stream ecology. Furthermore, coherent structures in a turbulent flow can lead to scour around hydraulic structures such as bridge piers [*Khosronejad et al.*, 2012] and can lead to bridge failure [*Briaud et al.*, 1999].

The transport of biogenic particles such as pollen [*Di-Giovanni and Kevan*, 1991], fungal spores [*Aylor*, 1990; *Brown and Hovmøller*, 2002], and seeds [*Nathan et al.*, 2002] is also a relevant question for ecology and plant pathology. The wind-borne dispersion of seeds is important for ecological issues such as gene flow, plant colonization, and the spread of invasive species [e.g. *Cain et al.*, 2000; *Nathan and Muller-Landau*, 2000; *Nathan et al.*, 2002]. Pollen dispersion from field crops has become a topic of interest in recent years, in order to quantify the probability of gene flow from genetically modified (GM) to non-GM wind-pollinated crops such as maize (*Zea mays*) [*Aylor*, 2002; *Aylor et al.*, 2003]. The turbulent dispersion of biogenic gases, such as pheromones, is known to be significant for the lifecycle of insect pests, such as the gypsy moth (*Lymantria dispar*) [*Aylor et al.*, 1976]. In addition, many diseases affecting field crops are carried by fungal spores [*Brown and Hovmøller*, 2002], which may be transported long distances after being entrained from plant leaves or stalks [*Aylor and Parlange*, 1975].

While some regional-scale studies have demonstrated that local flow patterns caused by topography can enhance the long-distance dispersion of heavy particles such as pollen [e.g. *Helbig et al.*, 2004], and recent large eddy simulation (LES) studies of particle dispersion within and above plant canopies have considered complexities such as finite size area sources [*Chamecki*, 2012], unstable stratification [*Pan et al.*, 2013], plant reconfiguration [*Pan et al.*, 2014], and edge effects [*Pan et al.*, 2015], many questions regarding the effects of topography on the dispersal of biogenic particles remain to be explored.

A variety of approaches have been employed in previous numerical studies of the transport of heavy particles over topography. Many previous studies [e.g. *Demuren and Rodi*, 1986; *Wu et al.*, 2000; *Zedler and Street*, 2001; *Gauer*, 2001; *Nagata et al.*, 2005; *Roulund et al.*, 2005; *Ortiz and Smolarkiewicz*, 2006, 2009] have used boundary-fitted grids. When this approach is used for simulations where the surface is allowed to evolve, remeshing will be required every time the surface deforms due to erosion or deposition. A number of numerical issues are associated with remeshing, including decreased numerical accuracy as the simulation progresses [*Khosronejad et al.*, 2011]. Furthermore, grid generation can be a challenge in complex domains [*Mittal and Iaccarino*, 2005; *Khosronejad et al.*, 2011].

Other studies of particle transport in turbulent flows have employed a Lagrangian approach where the governing equations of particle motion are solved directly for an ensemble of particles [e.g. *Shao and Li*, 1999; *Vinkovic et al.*, 2006; *Dupont et al.*, 2013; *Zwaafink et al.*, 2014; *Finn et al.*, 2016]. While this approach is advantageous for studying near-surface processes in detail (e.g. particle entrainment, saltation, and rebound), Lagrangian methods currently are too expensive to use for studies of bedform evolution [*Sotiropoulos and Khosronejad*, 2016] due to the large number of particles (\sim billions) required to converge statistics; the saltation layer in drifting snow or sand can carry on the order of 1.5×10^6 particles m^{-2} [*Gauer*, 2001].

Although immersed boundary LES of sediment transport has been conducted recently in an Eulerian framework [*Khosronejad and Sotiropoulos*, 2014], most studies of snow transport to date have been conducted following the Reynolds-averaged Navier Stokes (RANS) approach, where all scales of turbulence are parameterized [e.g. *Gauer*, 2001; *Lehning et al.*, 2008; *Schneiderbauer and Prokop*, 2011] or in LES using Lagrangian particles [*Zwaafink et al.*, 2014].

In this article we present a new approach for modeling the transport and deposition of heavy particles over surface topography in LES—applicable to a diverse set of problems including snow and sediment transport and the dispersion of heavy particles and passive scalars in complex terrain and urban environments. An immersed boundary version of an existing large eddy simulation code [*Albertson and Parlange*, 1999; *Kumar et al.*, 2006] for momentum is coupled with a Eulerian particle code [*Chamecki et al.*, 2009] that solves the advection-diffusion equation for heavy particles that includes gravitational settling and inertia. The particle mass conservation equation is discretized in a finite volume framework. In order to ensure mass conservation, we employ a Cartesian cut cell method [e.g. *Udaykumar et al.*, 1996; *Ye et al.*, 1999; *Udaykumar et al.*, 2001; *Ingram et al.*, 2003; *Mittal and Iaccarino*, 2005] where the finite volumes intersected by the fluid-solid interface are reshaped, i.e. the face area and volume fractions of a cut cell that lie in the fluid are accounted for explicitly in the discretized version of the mass conservation equation. We also modify the conservative interpolation scheme developed by *Chamecki et al.* [2008] to ensure that the interpolated velocity on the faces of the cut cells remains divergence-free. In addition, the wall models for particle deposition and erosion are modified to account for the possibility of a sloping surface.

This article is organized as follows. A description of the large eddy simulation model is presented in Sec. 2, including the new developments required to accurately simulate particle transport and deposition over surface topography. In Sec. 3, a validation case is presented where LES results are compared with wind tunnel experiments of particle deposition over topography. In Sec. 4, we present a case study of snow deposition over idealized surface topography, and use the LES to investigate how topography influences deposition patterns. A discussion of our results and the main conclusions will be presented in Sec. 5.

2. Model description

2.1. Large Eddy Simulation Code

The large eddy simulation code used in this study (discussed in detail by *Albertson and Parlange* [1999] and *Kumar et al.* [2006]) solves the three-dimensional filtered momentum equation written in rotational form. The governing equations are discretized using a pseudospectral collocation approach for horizontal derivatives, and second-order centered finite differences in the vertical, with the fully-explicit second-order Adams Bashforth method used for time integration. Nonlinear terms are fully dealiased using the 3/2 rule [e.g. *Canuto et al.*, 2012]. The resulting system of algebraic equations is solved using a fractional step method [*Chorin*, 1968]. In the simulations considered herein, we will compare the performance of several subgrid models in the context of particle transport and deposition, including the static Smagorinsky model [*Smagorinsky*, 1963], the plane-averaged dynamic model [*Lilly*, 1992], and the Lagrangian scale-dependence dynamic (LASD) model [*Bou-Zeid et al.*, 2005], which applies the dynamic procedure [*Lilly*, 1992] by

averaging over Lagrangian trajectories of fluid parcels [Meneveau *et al.*, 1996] to determine a value of the Smagorinsky coefficient while relaxing the scale invariance assumption of the model coefficient c_s , which is especially important in the near-wall region. Periodic boundary conditions are used in the horizontal directions; at the domain top, stress-free and zero vertical velocity conditions are imposed. The wall model (used over flat, horizontal homogeneous surfaces with no immersed boundary) is based on imposing Monin-Obukhov similarity in a local sense [Kumar *et al.*, 2006] with a test filter applied at scale 2Δ to better reproduce the mean surface stress [Bou-Zeid *et al.*, 2005]. In the present work we perform neutrally-stratified simulations of a turbulent half-channel, forcing with a constant pressure gradient force in the streamwise direction.

2.2. Immersed Boundary Method

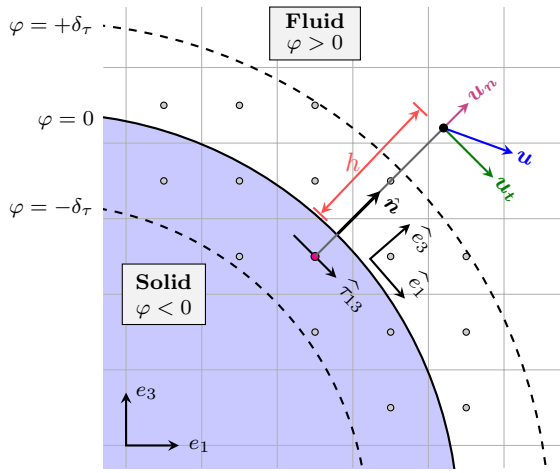


Figure 1. A schematic diagram illustrating the immersed boundary method for momentum. The wall model is applied in a band on nodes in the range $-\delta_\tau \leq \varphi \leq +\delta_\tau$, where φ is the level set function, $\hat{\mathbf{n}}$ is the surface normal vector, \mathbf{e}_i and $\hat{\mathbf{e}}_i$ represent the basis vectors in the Cartesian and local coordinate systems respectively, \mathbf{u} is the velocity vector calculated by trilinear interpolation at distance h from the wall, $\mathbf{u}_n = (\mathbf{u} \cdot \hat{\mathbf{n}}) \hat{\mathbf{n}}$ is the normal velocity component, $\mathbf{u}_t = \mathbf{u} - (\mathbf{u} \cdot \hat{\mathbf{n}}) \hat{\mathbf{n}}$ is the tangential velocity component, and $\hat{\tau}_{13}$ is the surface shear stress in the local coordinate system.

Surface topography is represented in the LES using an immersed boundary method (IBM) following the discrete direct forcing approach [Mohd-Yusof, 1997; Mittal and Iaccarino, 2005]. The use of an immersed boundary method, as opposed to other methods of representing surface topography (such as terrain-following coordinates or unstructured grids), has the advantages of easy and computationally inexpensive implementation, since the underlying discretization is still done on a Cartesian grid. Our implementation of the IBM is similar to that employed by Chester *et al.* [2007], and will be summarized below.

The interface between the fluid and the solid is represented in the code using a level set (φ), a signed distance function. The level set is zero at the solid-fluid interface ($\varphi = 0$), negative inside the solid ($\varphi < 0$), and positive in the fluid ($\varphi > 0$). The outward-facing normal vector on the surface is related to the level set function via

$$\hat{\mathbf{n}} = \frac{\nabla \varphi}{|\nabla \varphi|}. \quad (1)$$

Because the LES is not a wall-resolving simulation, a wall model must be used in the region near the immersed boundary interface in order to recover the correct velocity profile. The wall model for the surface shear stress is implemented in the band $-\delta_\tau \leq \varphi \leq +\delta_\tau$, where $\delta_\tau = 1.1 \Delta z$. The wall model in this band is imposed according to the following steps (a schematic diagram can be found in Fig. 1):

Step 1 For each grid node in the band $|\varphi| \leq \delta_\tau$, the velocity vector \mathbf{u} is calculated at a point $h = 1.5 \Delta z$ away from the wall in the direction of the normal vector $\hat{\mathbf{n}}$ using trilinear interpolation.

Step 2 A local (wall-relative) coordinate system is defined using $\hat{\mathbf{n}}$ and the tangential velocity component $\mathbf{u}_t = \mathbf{u} - (\mathbf{u} \cdot \hat{\mathbf{n}}) \hat{\mathbf{n}}$, via:

$$(\hat{\mathbf{e}}_1, \hat{\mathbf{e}}_2, \hat{\mathbf{e}}_3) = \left(\frac{\mathbf{u}_t}{|\mathbf{u}_t|}, \hat{\mathbf{n}} \times \hat{\mathbf{e}}_1, \hat{\mathbf{n}} \right). \quad (2)$$

Step 3 The SGS shear stress in this local coordinate system is calculated as:

$$\hat{\tau}_{13} = -\rho \left[\frac{\kappa |\mathbf{u}_t|}{\ln(h/z_0)} \right]^2, \quad (3)$$

where $\kappa = 0.4$ is the von Kármán constant, z_0 is the roughness length, and $h = 1.5 \Delta z$ is the distance from the wall.

Step 4 The SGS shear stress is transformed back to the Cartesian coordinate system of the LES grid via:

$$\tau_{ij} = a_{in} \hat{\tau}_{nm} a_{mj} \quad (4)$$

where a_{in} and a_{jm} are the direction cosines, e.g. $a_{in} = \mathbf{e}_i \cdot \hat{\mathbf{e}}_n$, and $(\mathbf{e}_1, \mathbf{e}_2, \mathbf{e}_3)$ are the basis vectors in the Cartesian frame of reference.

At each timestep, the velocity field inside the immersed boundary ($\varphi < 0$) is set to zero, then polynomial smoothing is applied inside the IBM surface to reduce the Gibbs oscillations that arise due to the spectral differentiation in horizontal directions. This is done prior to the pressure solver, which enforces incompressibility ($\nabla \cdot \mathbf{u} = 0$) of the velocity field.

2.3. Finite-Volume Particle Code

In order to avoid the large computational overhead associated with including a large number of Lagrangian particles in the LES required to converge statistics, an Eulerian framework is adopted here, an approach that has been used successfully to model diverse problems including the dispersion of heavy particles in the atmospheric boundary layer [Dupont *et al.*, 2006; Chamecki *et al.*, 2009; Chamecki and Meneveau, 2011; Pan *et al.*, 2013; Freire *et al.*, 2016], sediment transport [Zedler and Street, 2001; Chou and Fringer, 2008; Khosronejad and Sotiropoulos, 2014], gravity currents [Necker *et al.*, 2002], snow transport [Lehming *et al.*, 2008], and oil plumes in ocean turbulence [Yang *et al.*, 2015; Chen *et al.*, 2016]. The evolution of the particle concentration field is represented using an advection-diffusion equation, given as:

$$\frac{\partial \tilde{C}}{\partial t} + \nabla \cdot (\tilde{\mathbf{v}}_p \tilde{C}) = -\nabla \cdot \boldsymbol{\pi}^C + Q_{src}. \quad (5)$$

Here \tilde{C} is the resolved particle concentration field, $\tilde{\mathbf{v}}_p$ is the particle advection velocity, $\tilde{\mathbf{u}}$ is the resolved velocity field, Q_{src} is a source term (e.g. for point or area source releases), and $\boldsymbol{\pi}^C$ is the SGS particle concentration flux, defined as

$$\boldsymbol{\pi}^C = \tilde{\mathbf{u}} \tilde{C} - \tilde{\nabla} \tilde{C}, \quad (6)$$

and modeled using a flux-gradient model:

$$\boldsymbol{\pi}_{model}^C = -\frac{\nu_{sgs}}{Sc_{sgs}} \nabla \tilde{C}, \quad (7)$$

where $\nu_{sgs} = (c_s \Delta)^2 |\tilde{\mathbf{S}}|$ is the SGS eddy viscosity, Δ is the LES filter width, $\tilde{S}_{ij} = \frac{1}{2} \left(\frac{\partial \tilde{u}_i}{\partial x_j} + \frac{\partial \tilde{u}_j}{\partial x_i} \right)$ is the filtered strain rate tensor, $|\tilde{\mathbf{S}}| = (2\tilde{S}_{ij}\tilde{S}_{ij})^{1/2}$ is its magnitude, c_s is the Smagorinsky coefficient, and Sc_{sgs} is the SGS Schmidt number, which for our present simulations is assumed to be constant. The particle advection velocity is defined as

$$\tilde{\mathbf{v}}_p = \tilde{\mathbf{u}} + \tau_p \mathbf{g} - \tau_p \tilde{\mathbf{a}}, \quad (8)$$

where the terms on the right hand side represent contributions from the fluid velocity, gravitational settling, and particle inertia respectively. Here τ_p is a characteristic particle timescale, \mathbf{g} is the gravity vector, and $\tilde{\mathbf{a}}$ is the particle acceleration vector. The gravitational settling term is expressed as $\tau_p \mathbf{g} = -w_s \mathbf{e}_3$, where w_s is a mean settling velocity for the particles, which in the present study are assumed to be monodisperse. Thus, the particle timescale is given as $\tau_p = w_s/g$.

The inertia term is modeled by replacing the particle acceleration by the fluid acceleration [e.g. *Shotorban and Balachandar, 2007; Balachandar and Eaton, 2010*], i.e.

$$\tilde{\mathbf{a}} = \frac{D\tilde{\mathbf{u}}}{Dt} = -\nabla \tilde{p}^* + \frac{1}{2} \nabla (\tilde{\mathbf{u}} \cdot \tilde{\mathbf{u}}), \quad (9)$$

where \tilde{p}^* is the modified pressure that enforces incompressibility. Here $(\tilde{\cdot})$ denotes the test filtering operation at scale 2Δ ; we find that in simulations of inertial particles over an immersed boundary, test filtering of the fluctuating pressure gradient term reduces nonphysical oscillations that occur in particle deposition (due to the Gibbs oscillations that appear in the modified pressure and its derivatives). Note that the contribution from the divergence of the SGS stress tensor is neglected in (9) due to the fact that only a small amount of energy is contained in the SGS scales, and because τ_p is small in the equilibrium assumption [e.g. *Shotorban and Balachandar, 2007; Yang et al., 2016*].

Because *Chamecki et al. [2009]* were interested in the dispersion of heavy particles from point or area sources (which can lead to strong spatial gradients), they discretized (5) in a finite volume framework rather than employing the pseudospectral approach often used in LES. The discrete version of (5) on a Cartesian grid over a flat surface (i.e. with no immersed boundary), written here for one Euler time step, is given as:

$$\begin{aligned} & \frac{\tilde{C}_{i,j,k}^{n+1} - \tilde{C}_{i,j,k}^n}{\Delta t} = \\ & -\frac{1}{\Delta x} [F_{i+1/2,j,k} - F_{i-1/2,j,k}] - \frac{1}{\Delta y} [F_{i,j+1/2,k} - F_{i,j-1/2,k}] \\ & - \frac{1}{\Delta z} [F_{i,j,k+1/2} - F_{i,j,k-1/2}] + \frac{Q_{src}}{V_{cell}}, \quad (10) \end{aligned}$$

where $\tilde{C}_{i,j,k}^n$ is the concentration in cell (i, j, k) at time $t = n\Delta t$, $F_{i,j,k}$ denotes the sum of the advective and SGS diffusive fluxes on a face of the control volume, and $V_{cell} = \Delta x \Delta y \Delta z$ is the volume of a cell. The face-averaged fluxes are calculated as (e.g. for the east x -face of a control volume):

$$F_{i+1/2,j,k} = [U_{i+1/2,j,k} C_{i+1/2,j,k}] - \left[K_{i+1/2,j,k} \frac{1}{\Delta x} (C_{i+1,j,k} - C_{i,j,k}) \right] \quad (11)$$

where the first term is the advective flux, the second term is the SGS diffusive flux, and $K_{i,j,k} = \nu_{i,j,k}^{sgs}/Sc_{sgs}$ is the SGS diffusivity for particles.

The interpolation of particle concentration to the faces of the control volumes is done using SMART, a bounded third-order upwind scheme proposed by *Gaskell and Lau [1988]*, which prevents nonphysical negative concentrations. The velocity interpolation is done using the conservative interpolation scheme proposed by *Chamecki et al. [2008]*, which ensures that the interpolated velocity field on the finite volume faces remains divergence-free. A discussion of how the finite volume spatial discretization is modified for use with the immersed boundary method can be found in Sec. 2.4.

The lower boundary condition for particle concentration is derived based on the assumption of equilibrium between gravitational settling and turbulent diffusion [*Chamberlain, 1967; Kind, 1992*], which was later modified by *Freire et al. [2016]* to account for thermal stratification. In the present study, we consider only neutral stratification. The total particle concentration flux at the wall can be separated into a deposition term and a source term [*Chamecki et al., 2009*]:

$$\Phi_{sgs}(x, y) = \Phi_{sgs}^{src}(x, y) + \Phi_{sgs}^{dep}(x, y), \quad (12)$$

where

$$\Phi_{sgs}^{src}(x, y) = w_s C_r \left(\frac{z_1}{z_r} \right)^{-\gamma} \left[1 - \left(\frac{z_1}{z_r} \right)^{-\gamma} \right]^{-1} \quad (13)$$

and

$$\Phi_{sgs}^{dep}(x, y) = -w_s \tilde{C}(x, y, z_1) \left[1 - \left(\frac{z_1}{z_r} \right)^{-\gamma} \right]^{-1}. \quad (14)$$

In (13)–(14), $z_1 = \Delta z/2$ is the height of the first node where \tilde{C} is stored (in the LES we employ a staggered grid arrangement, where \tilde{C} is collocated with the u and v velocity components and pressure, whereas w is stored $\Delta z/2$ above and below the uvp nodes), and z_r is a height where a reference concentration C_r is imposed. Here we take $z_r = z_{0,c}$, i.e. we use the roughness height for particle concentration as the reference height. The quantity γ , given as

$$\gamma = \frac{Sc_T w_s}{\kappa u_*} \quad (15)$$

is a dimensionless parameter (known as the Rouse number) that represents the relative importance of turbulent diffusion and gravitational settling, where Sc_T is the turbulent Schmidt number, which is not necessarily equal to the SGS Schmidt number Sc_{sgs} . Here we adopt a value of $Sc_T = 0.95$, which in the limit $w_s \rightarrow 0$, recovers the commonly accepted form [*Högström, 1988*] of the Monin-Obukhov similarity function for scalars [*Chamecki et al., 2009*].

2.4. Cartesian Cut Cell Method for Particle Concentration

In order to ensure explicit conservation of mass in the particle phase, we use a Cartesian cut cell method to discretize the particle concentration equation in the finite volume framework when an immersed boundary is present. In Cartesian cut cell methods [e.g. *Udaykumar et al., 1996; Ye et al., 1999; Udaykumar et al., 2001; Ingram et al., 2003; Mittal and Iaccarino, 2005*], finite volume cells intersected by the immersed boundary surface (i.e. the zero level set) are reshaped to ensure that the integral form of the conservation equation is satisfied explicitly in these irregularly shaped (non-Cartesian) cells. This is done by introducing

the volume fraction of each cell and the area fraction of each face in the fluid into the discretized version of the particle mass conservation equation.

2.4.1. Discretization in Cut Cell Framework

In the Cartesian cut cell framework, the discrete version of the particle mass conservation equation (10), again written for one Euler step, becomes:

$$\begin{aligned} \frac{\tilde{C}_{i,j,k}^{n+1} - \tilde{C}_{i,j,k}^n}{\Delta t} = & -\frac{1}{\alpha_{i,j,k} \Delta x} [A_{i+1/2,j,k}^x F_{i+1/2,j,k} - A_{i-1/2,j,k}^x F_{i-1/2,j,k}] \\ & -\frac{1}{\alpha_{i,j,k} \Delta y} [A_{i,j+1/2,k}^y F_{i,j+1/2,k} - A_{i,j-1/2,k}^y F_{i,j-1/2,k}] \\ & -\frac{1}{\alpha_{i,j,k} \Delta z} [A_{i,j,k+1/2}^z F_{i,j,k+1/2} - A_{i,j,k-1/2}^z F_{i,j,k-1/2}] \\ & + \frac{Q_{src}}{\alpha_{i,j,k} V_{cell}} + \frac{S_{i,j,k}^\Gamma}{\alpha_{i,j,k} V_{cell}} (\hat{\Phi}_{sgs}^{dep} + \hat{\Phi}_{sgs}^{src}). \end{aligned} \quad (16)$$

In (16), $\alpha_{i,j,k}$ is the volume fraction of a cut cell in the fluid, i.e. $\alpha = 1$ for a regular cell fully in the fluid, $0 < \alpha < 1$ for a cut cell, and $\alpha = 0$ for a cell fully in the solid. (Note that, in practice, the right-hand side of (16) is set to zero at each timestep in the code in cells where $\alpha = 0$ to avoid division by zero). The fluxes on the finite volume faces are modified by the fraction of the face in the fluid, e.g. $A_{i+1/2,j,k}^x$ for the east x -face, where $0 < A^x, A^y, A^z < 1$. The relationship between the face areas (\bar{S}^x , \bar{S}^y , and \bar{S}^z) and the face area fractions is

$$\begin{aligned} S_{i,j,k}^x &= \Delta y \Delta z A_{i,j,k}^x \\ S_{i,j,k}^y &= \Delta x \Delta z A_{i,j,k}^y \\ S_{i,j,k}^z &= \Delta x \Delta y A_{i,j,k}^z. \end{aligned} \quad (17)$$

The wall models for erosion ($\hat{\Phi}_{sgs}^{src}$) and deposition ($\hat{\Phi}_{sgs}^{dep}$) are modified for the cut faces, which are not necessarily perpendicular to the gravity vector; these will be discussed below. Here S^Γ denotes the dimensional area of the cut face. A schematic diagram of the face areas and cut face in a cut cell can be found in Fig. 2. For the details of how the geometric quantities (face area fractions, cell volume fractions, cut face area, and cut face normal vector) required for the cut cell method are calculated from the level set function φ , the reader is referred to Appendix A.

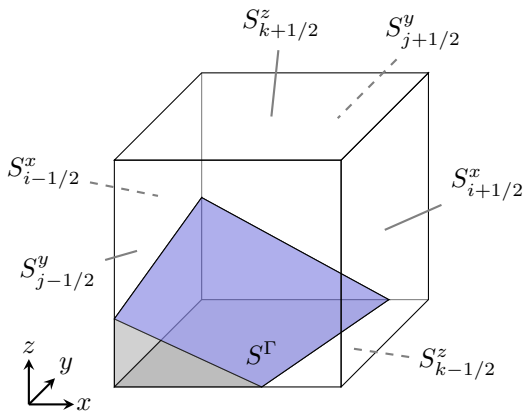


Figure 2. A schematic diagram of the regular face (S_x , S_y , and S_z) and cut face (S_Γ) areas in a cut cell.

2.4.2. Wall Models

In the Cartesian cut cell framework, the wall models for particle erosion and deposition must be modified to account for the possibility of an inclined surface (i.e. where the sur-

face is no longer perpendicular to the gravity vector). In this case, the deposition model (14) becomes:

$$\hat{\Phi}_{sgs}^{dep} = -(\cos \beta) w_s \tilde{C} \left[1 - \left(\frac{h}{z_r} \right)^{-\hat{\gamma}} \right]^{-1}. \quad (18)$$

where $\beta = \cos^{-1}(\mathbf{e}_3 \cdot \hat{\mathbf{n}})$ is slope angle of the cut face, and $\hat{\gamma} = Sc_\Gamma w_s / \kappa \hat{u}_*$ is the Rouse number based on the local shear stress $\hat{u}_* = \sqrt{-\hat{\tau}_{13}} / \rho$, which is calculated according to (3). Note that one can recover the standard wall model for particle deposition over a flat surface (14) when $\beta = 0$. Conversely, when $\beta = \pi/2$ (a vertical wall), $\hat{\Phi}_{sgs}^{dep} = 0$. Here we only consider deposition due to gravitational settling, and neglect the contribution from impaction, which is expected to be negligible for our present simulations; this assumption will be discussed more below.

Similarly, the erosion model on a cut face is given as:

$$\hat{\Phi}_{sgs}^{src} = (\cos \beta) \hat{w}_s C_r \left(\frac{h}{z_r} \right)^{-\hat{\gamma}} \left[1 - \left(\frac{h}{z_r} \right)^{-\hat{\gamma}} \right]^{-1} \quad (19)$$

where we once again use the wall-relative versions of u_* and γ . In the present article, we consider only the case of deposition, and do not let particles erode once they deposit. A parameterization of the saltation layer through the wall model will be addressed in a future study.

2.4.3. Small Cell Treatment

One well-known challenge associated with Cartesian cut cell methods is the need to reduce the timestep in order to satisfy the local Courant-Friedrichs-Lewy (CFL) condition in cut cells with small volume fractions. For an explicit time advancement scheme as we adopt here, the timestep must satisfy the condition $C = u \Delta t / \Delta \ell < 1$ to avoid numerical instabilities, that is, the timestep Δt must be less than the characteristic convection time $\Delta \ell / u$. For cut cells with small volume fractions, the characteristic cell lengthscale $\Delta \ell$ will be much smaller than the grid spacing (Δx , Δy , or Δz), thus requiring a much smaller timestep to ensure the CFL condition is satisfied.

While a number of approaches have been proposed to circumvent this issue (allowing investigators to use the same timestep as for the regular Cartesian grid) including cell linking [e.g. Kirkpatrick *et al.*, 2003], cell merging [e.g. Ye *et al.*, 1999], or blended approaches [e.g. Hartmann *et al.*, 2008], we use the conservative mixing procedure proposed by Hu *et al.* [2006] and extended to three-dimensional simulations by Meyer *et al.* [2010]. The conservative mixing procedure is applied only in small cells (i.e. where $\alpha < 0.5$), which are identified during the geometric calculations. After calculating the RHS of (16), and AB2 time advancement, the particle concentration in a small cell is mixed with the seven neighboring cells in the direction of the cut face normal vector \mathbf{n}^Γ . The conservative mixing procedure conserves mass, and allows us to use the normal timestep we would employ for a given Cartesian grid. A summary of our implementation of the conservative mixing model can be found in Appendix B.

2.4.4. Velocity Interpolation

At each timestep, the velocity field calculated from the LES must be interpolated to the finite volume faces in order to calculate the advective and diffusive fluxes on the faces of each control volume. One important constraint on the interpolation method is the requirement that the interpolated velocity field remain divergence-free; this is critical in order to conserve mass in the particle phase. The conservative interpolation method proposed by Chamecki *et al.* [2008] does not guarantee that the interpolated velocity field will

be divergence-free in cut cells. In fact, the discrete version of the continuity equation that must be satisfied in cut cells (where $0 < \alpha < 1$) must include the face area fractions in the discrete divergence operator, i.e.

$$\begin{aligned} \nabla \cdot \mathbf{u}_{int} = & \frac{1}{\Delta x} [A_{i+1/2}^x U_{i+1/2} - A_{i-1/2}^x U_{i-1/2}] + \\ & \frac{1}{\Delta y} [A_{j+1/2}^y V_{j+1/2} - A_{j-1/2}^y V_{j-1/2}] + \\ & \frac{1}{\Delta z} [A_{k+1/2}^z W_{k+1/2} - A_{k-1/2}^z W_{k-1/2}] = 0, \end{aligned} \quad (20)$$

where \mathbf{u}_{int} is the interpolated velocity. For brevity of notation, unnecessary indicies are omitted from (20) and the following discussion, i.e. we will write $A_{i+1/2}$ rather than $A_{i+1/2,j,k}$, etc.

In order to enforce the divergence-free condition in the cut cells, we first calculate an intermediate interpolated velocity field using the conservative interpolation method proposed by *Chamecki et al.* [2008]. Then, we remove the finite divergence using a projection method. We first solve the Poisson equation

$$\nabla^2 \psi = \nabla \cdot \mathbf{u}_{int}^* \quad (21)$$

where \mathbf{u}_{int}^* is the intermediate interpolated velocity with finite divergence in cut cells, then the divergence-free interpolated velocity field that satisfies (20) is then calculated via

$$\mathbf{u}_{int} = \mathbf{u}_{int}^* - \nabla \psi. \quad (22)$$

Note that in (21), the discrete divergence and Laplace operators must include the face area fractions in the cut cell framework. The right hand side of (21) is discretized as in (20), and the Laplacian is discretized using second-order centered differences:

$$\begin{aligned} \nabla^2 \psi = & \frac{1}{(\Delta x)^2} [A_{i+1/2}^x \psi_{i+1} - (A_{i+1/2}^x + A_{i-1/2}^x) \psi_i + A_{i-1/2}^x \psi_{i-1}] + \\ & \frac{1}{(\Delta y)^2} [A_{j+1/2}^y \psi_{j+1} - (A_{j+1/2}^y + A_{j-1/2}^y) \psi_j + A_{j-1/2}^y \psi_{j-1}] + \\ & \frac{1}{(\Delta z)^2} [A_{k+1/2}^z \psi_{k+1} - (A_{k+1/2}^z + A_{k-1/2}^z) \psi_k + A_{k-1/2}^z \psi_{k-1}]. \end{aligned} \quad (23)$$

Note that one recovers the standard stencils for second-order centered differences in (20) and (23) in the case of cells fully in the fluid, where all of the face area fractions are identically unity ($A^x = A^y = A^z = 1$). The discrete version of (21) is solved iteratively at each timestep using the BiCGSTAB(2) algorithm [*Sleijpen and Fokkema*, 1993] as described in *Van der Vorst* [2003].

3. Comparison with Wind Tunnel Data

In order to validate the proposed numerical model, we designed simulations to compare our LES results with an experimental study of particle deposition over topography conducted in a wind tunnel [*Goossens*, 2006]. The detailed deposition measurements in this study make it an ideal test case to validate our LES model. A summary of the wind tunnel experiments of *Goossens* [2006] can be found in Sec. 3.1; a description of the simulations used for the validation cases and a comparison with the experimental data can be found in Sec. 3.2.

3.1. Wind tunnel experiments of *Goossens* [2006]

The particle deposition experiments of *Goossens* [2006] were conducted in a closed-return wind tunnel with a test section of dimensions 7.6 m long, 1.2 m wide, and 0.60 m

high. Dust was released in the return section of the wind tunnel, and three separate concave-convex symmetric hills were constructed out of zinc plates in order to study the deposition patterns over these topographic features. For our validation case described below in Sec. 3.2, we compare our LES results to deposition onto the hill (“hill 2”) having dimensions of height $H = 0.03$ m and length $L = 0.06$ m. The turbulent boundary layer (as measured 0.5 m upstream of each hill) was characterized by free stream velocity of $U_\infty = 1.72$ m s⁻¹, friction velocity $u_* = 0.06$ m s⁻¹, and roughness length $z_0 = 1 \times 10^{-5}$ m (i.e. the surface was hydrodynamically smooth). The Reynolds number based on hill height (sometimes called the “roughness Reynolds number”) for hill 2 was $Re_h = u_* h / \nu = 123$; *Cermak* [1984] found that Reynolds-number independence for wind tunnel studies of flows over topography was achieved for $Re_h > 70$; therefore the Reynolds number criterion was found to be satisfied. Each hill was placed in the wind tunnel with a fetch of 5.05 m from the beginning of the test section to the beginning of the hill.

Dust particles were released in the return section of the wind tunnel at a rate of 13 kg h⁻¹; the dust used in the experiment was prepared from calcareous loam with a mean particle diameter of $\bar{d}_p = 42$ μ m, maximum particle size of $d_p^{max} = 104$ μ m, and a mass density of $\rho_p = 2650$ kg m⁻³. *Goossens* [2006] notes that the resuspension of particles was expected to be small due to the small friction velocity. Deposition was measured at 0.01 m increments at 250 locations in the longitudinal direction and as a function of particle size for nine grain size classes. Each particle release experiment was 12 minutes in duration.

3.2. Large eddy simulations

Large eddy simulations with heavy particle deposition over surface topography were conducted in order to validate the proposed numerical model with the wind tunnel data of *Goossens* [2006]. Neutral flow simulations were driven by a constant pressure gradient force, and a two-dimensional sinusoidal hill (spanning the entire domain in the y -direction), described by

$$h(x) = H \cos^2 \left(\frac{\pi(x - x_0)}{2L} \right) \quad (24)$$

was included in the simulations, where H is the hill height, L is the hill length, and x_0 is the streamwise coordinate of the hill crest. Simulations were run at a coarse ($64 \times 32 \times 48$) and fine ($128 \times 64 \times 96$) resolution, and using three sub-grid models—static Smagorinsky [*Smagorinsky*, 1963] with $c_s = 0.10$ and wall damping included [e.g. *Mason*, 1994], the plane-averaged dynamic model [*Lilly*, 1992], and the Lagrangian-averaged scale-dependent dynamic Smagorinsky model [*Bou-Zeid et al.*, 2005] in order to compare the effects of grid resolution and SGS model on the observed deposition patterns.

Particles were released from an area source in the y - z plane near the leading edge of the domain (at node $jx = 3$), with a release rate of $Q = 3.61$ g s⁻¹ (13 kg h⁻¹). Simulation results were compared to the data for the 31–41 μ m size class from *Goossens* [2006]. (Note that *Goossens* [2006] found the normalized particle deposition patterns did not vary greatly for the different particle size classes). Periodic boundary conditions were employed for the concentration field in the y -direction and inflow/outflow conditions in the x -direction.

Particle settling velocity was calculated from Stokes’ drag law

$$w_s = \frac{\rho_p g d_p^2}{18 \mu_{air}}, \quad (25)$$

Table 1. Simulation properties for validation cases.

Quantity	Symbol	Coarse Resolution	Fine Resolution
Domain [m]	$L_x \times L_y \times L_z$	$1.28 \times 0.64 \times 0.24$	$1.28 \times 0.64 \times 0.24$
Number of gridpoints [-]	$N_x \times N_y \times N_z$	$64 \times 32 \times 48$	$128 \times 64 \times 96$
Grid spacing [m]	$\Delta x \times \Delta y \times \Delta z$	$0.02^2 \times 0.005$	$0.01^2 \times 0.0025$
Timestep, Smag [s]	Δt	1.5×10^{-3}	7.5×10^{-4}
Timestep, Dynamic [s]	Δt	1.5×10^{-3}	4.0×10^{-4}
Timestep, LASD [s]	Δt	1.5×10^{-3}	4.0×10^{-4}
Friction velocity [m s ⁻¹]	u_*	0.06	0.05
Characteristic timescale [s]	$T_\ell = L_z/u_*$	4.0	4.8
Duration of particle release [-]	nT_ℓ	$n = 30$	$n = 25$
Roughness length [m]	z_0	1.0×10^{-5}	1.0×10^{-5}
Settling velocity [m s ⁻¹]	w_s	0.10	0.10
SGS Schmidt number [-]	Sc_{sgs}	1.0	1.0
Hill height [m]	H	0.03	0.03
Hill length [m]	L	0.06	0.06
Hill centerline location [m]	x_0	0.64	0.64
Stokes number [-]	$St_H = \tau_p u_*/H$	0.02	0.017

which is valid for small particle Reynolds numbers ($Re_p = w_s d_p / \nu_{air}$), and where ρ_p is particle density and μ_{air} is the dynamic viscosity of air [e.g. *Pruppacher et al.*, 1998; *Lamb and Verlinde*, 2011]. For 36 μm particles, $Re_p \simeq 0.24$ and $w_s = 0.10 \text{ m s}^{-1}$. Note that using a semi-empirical formula [*Lamb and Verlinde*, 2011, pp. 388-390] to estimate w_s (the typical approach for large Re_p) yielded a similar estimate of settling velocity.

Simulations were spun up on a coarse grid with no particles for approximately 30 large-eddy turnover times, where $T_\ell = L_z/u_*$. Particles then were released for 25-30 T_ℓ (2 minutes physical time). In the case of the simulations on the fine grid, this was done after trilinear interpolation of the velocity field to the fine grid and evolving the velocity field for several T_ℓ . A summary of the properties of the simulations for the validation cases can be found in Table 1.

One well-known property of heavy particles in turbulent flow is the fact that particles will not follow fluid streamlines exactly due to their inertia. This effect can be quantified by the Stokes number, a dimensionless number defined as $St = \tau_p / \tau_f$, where τ_p is once again the characteristic particle timescale, and τ_f is a characteristic fluid timescale. In the $St \rightarrow \infty$ limit, the particles will settle without feeling the effect of the fluid; when $St \rightarrow 0$, the particles are passive tracers that follow the motion of the fluid exactly. The trajectory-crossing effect becomes significant for $St \sim \mathcal{O}(1)$.

Two variations of the Stokes number are relevant for the results presented here. The first is the grid Stokes number $St_\Delta = \tau_p / \tau_\Delta$, where τ_Δ is the timescale of the smallest turbulent eddies resolved in an LES. Note that τ_Δ can be estimated via [e.g. *Yang et al.*, 2016]

$$\tau_\Delta \sim T_\ell \left(\frac{\Delta}{\ell} \right)^{2/3} \sim \frac{L_z}{u_*} \left(\frac{\Delta}{L_z} \right)^{2/3} \quad (26)$$

where ℓ and T_ℓ are respectively the integral length and time scales. As discussed by *Shotorban and Balachandar* [2007],

the equilibrium Eulerian approach (where the particle velocity can be explicitly computed from the fluid velocity field as we do in the present work) has been found to be valid up to $St_\Delta \lesssim 0.5$ from comparison with direct numerical simulation (DNS) results. For the present study, $St_\Delta \sim \mathcal{O}(0.01)$ for the validation cases presented in Sec. 3 and $St_\Delta \sim \mathcal{O}(1 \times 10^{-4})$ for the snow deposition case study presented in Sec. 4, demonstrating that it is reasonable to adopt the equilibrium Eulerian approach here.

The second relevant parameter is the Stokes number based on hill height and friction velocity, i.e. $St_H = \tau_p u_*/H$, which is the relevant parameter for characterizing the extent to which the trajectory-crossing effect enhances particle deposition. Previous studies of the deposition of inertial particles onto obstacles [e.g. *May and Clifford*, 1967; *Aylor*, 1982; *Moran et al.*, 2013] have used a Stokes number based on the characteristic velocity scale of the flow and obstacle length-scale (e.g. $St = \tau_p u_0 / \ell_0$) to characterize the role of particle inertia. For the present study, we define this Stokes number in terms of hill height and friction velocity; values for the simulations considered here are reported in Tables 1 and 2. Based on the fit by *Aylor* [1982] to the data of *May and Clifford* [1967] for the impaction of inertial particles onto cylinders in crossflow, i.e.

$$E_I = 0.86 (1 + 0.442 St^{-1.967})^{-1}, \quad (27)$$

the impaction efficiency for the largest value of St_H considered here ($St_H = 0.02$) is negligible, i.e. $E_I \sim \mathcal{O}(1 \times 10^{-3})$. (Note that impaction efficiency, where $0 \leq E_I \leq 1$, is simply the fraction of particles that will impact onto an obstacle due to the trajectory-crossing effect). Thus neglecting the contribution from impaction in the wall model for particle deposition (18) is a reasonable assumption for the range of St_H considered here.

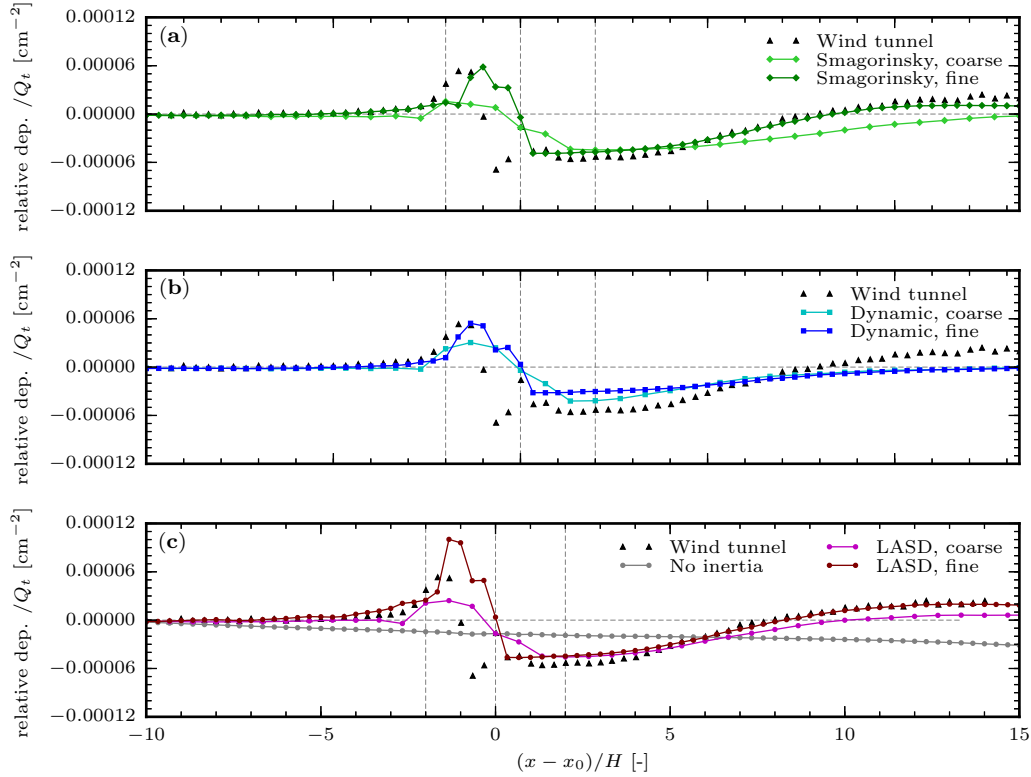


Figure 3. Particle deposition over topography from the LES at coarse ($64 \times 32 \times 48$) and fine ($128 \times 64 \times 96$) resolution, together with the wind tunnel data of *Goossens* [2006]. Here relative deposition, normalized by the total mass of particles released (Q_t) is plotted as a function of distance relative to the streamwise location of the hill crest (x_0), normalized by hill height (H). (a) Static Smagorinsky model with $c_s = 0.1$ (b) plane-average dynamic model (c) Lagrangian scale-dependent dynamic model.

3.3. Particle deposition

A comparison between the LES and the wind tunnel data can be found in Fig. 3. Results from the static Smagorinsky SGS model can be found in panel (a), the plane-averaged dynamic model in panel (b), and the Lagrangian scale-dependent dynamic model in panel (c). In each panel, the relative deposition is normalized by the total mass of particles released (Q_t) and plotted as a function of normalized distance from the streamwise location of the hill crest (x_0). Following *Goossens* [2006], we define the relative deposition as the deposition with the mean upwind of the hill (from $(x - x_0) \in [-50, 10]$ cm) removed. One can see from Fig. 3 that the relative deposition from the wind tunnel data increases on the windward side of the hill, then decreases rapidly on the leeward side. Downwind of the hill, the relative depo-

sition is initially negative, but increases downstream of the hill, and becomes positive at $(x - x_0) \approx 7H$ (i.e. deposition is larger here than what is found upwind of the hill). This same qualitative pattern of particle deposition over hills has been observed both in the field and in experimental studies at various scales [*Goossens*, 2006].

On the coarse ($64 \times 32 \times 48$) grid, all three SGS models recover the correct trends in the deposition pattern, where the maximum of deposition is found on the windward side of the hill, the minimum on the leeward side, and deposition increases going downwind of the hill in the wake. However, all three SGS models underpredict the peak of deposition on the windward side of the hill, and overpredict deposition on the leeward side.

On the fine ($128 \times 64 \times 96$) grid, the Smagorinsky model, displayed in Fig. 3(a) has a reasonable prediction of the deposition patterns compared to the wind tunnel data. On the windward side of the hill, the peak

of the deposition is slightly displaced, occurring closer to the hill crest than in the experimental data. However, the Smagorinsky model is in good agreement with the wind tunnel data on the leeward side of the hill, and in the wake, only beginning to deviate slightly around $x - x_0 \approx 10H$.

The plane-averaged dynamic model, as seen in Fig. 3(b), has a more accurate prediction of the peak of deposition on the windward side of the hill than Smagorinsky, although it also slightly displaces the peak of deposition toward the crest of the hill. However, here the dynamic model does not capture the behavior of the deposition in the wake as well as Smagorinsky, overpredicting deposition in the near wake, and underpredicting deposition in the far wake.

The deposition pattern from the LASD model, visible in Fig. 3(c), begins overpredicting deposition before the start of the hill (e.g. around $x - x_0 \approx 4H$). The LASD model significantly overpredicts the peak of deposition on the windward side of the hill. However, the LASD model successfully captures the deposition in the wake, here performing better than both the dynamic and Smagorinsky models. An additional simulation using the LASD model was run on the fine grid, but without the model for particle inertia (i.e. by omitting the $-\tau_p \tilde{\mathbf{a}}$ term in the particle advection velocity (8)). One can see that the curve for the no inertia case, displayed in Fig. 3(c) fails to recover the correct deposition patterns, demonstrating that accounting for particle inertia is critical when simulating the deposition of heavy particles over complex topography. The effects of particle inertia on the concentration field and deposition patterns will be discussed further in Sec. 4.

The overprediction of deposition on the windward side of the hill that is visible in Fig. 3(c) for the LASD model on the fine grid is likely related to the fact that the LASD model uses information inside the IBM interface (e.g. the velocity field that has been set to zero, then polynomial smoothing applied) when determining a value of the Smagorinsky coefficient c_s for nodes near the boundary; note that the LASD model uses test filters at scale 2Δ and 4Δ to determine c_s ; thus values of c_s (and consequently the SGS scalar diffusivity $K_c^{sgs} = (c_s \Delta)^2 |\tilde{\mathbf{S}}| / Sc_{sgs}$) on nodes near the IBM interface will be influenced by the nonphysical values of velocity within the immersed boundary surface. Nevertheless, on the fine grid the three SGS models considered are in reasonable agreement with the experimental data.

4. Case Study of Snow Deposition

In this section, we use the proposed numerical model to investigate the deposition of snow over idealized surface topography. As discussed earlier, most previous studies of snow transport have followed the RANS approach, where all scales of turbulence are parameter-

ized [Gauer, 2001; Schneiderbauer and Prokop, 2011], or have employed Lagrangian particle models and focused on drifting at small spatial scales [Zwaafink et al., 2014]. In a recent article, Lehning et al. [2008] focused on the extent to which topography modifies mean wind fields in complex terrain, thereby modifying the deposition velocity, leading to preferential deposition of snow. However, the effect of the spatially heterogeneous flow fields induced by surface topography and particle inertia on deposition patterns in the context of snow transport has not, to our knowledge, been explored using LES in an Eulerian framework.

4.1. Large eddy simulations

In order to investigate the effects of topography on snow deposition patterns (an important question for hydrological modeling, alpine ecology, and avalanche forecasting), we simulate the deposition of fresh snow, where particles are released from an area source in the x - y plane near the top of the domain. Idealized surface topography—here a two-dimensional sinusoidal hill extending across the entire domain in the y -direction, described by (24)—was included in the simulation. Here the roughness Reynolds number is approximately $Re_h \approx 2.6 \times 10^5$; thus Re_h independence is found to be satisfied. While snow deposition and transport in the real world can include a number of complexities, including saltation, non-neutral thermal stratification, erosion of snow once it is deposited, an evolving surface due to erosion and/or deposition, sublimation of blowing snow, fracturing and sintering of ice particles, and polydisperse particles, we here perform idealized simulations. We restrict ourselves to monodisperse particles (with a constant settling velocity w_s), neutral stratification, and a fixed surface height. Once particles deposit, they are not allowed to be resuspended.

Parameters for this simulation can be found in Table 2. The velocity field for these simulations was spun up on a coarse ($64 \times 32 \times 48$) grid, then interpolated to the finer ($128 \times 64 \times 96$) grid and evolved for several T_ℓ before beginning the particle release. The plane-averaged dynamic SGS model [Lilly, 1992] was employed. Both the spinup and particle release were one hour physical time in duration (approximately $7.6 T_\ell$). We used a settling velocity of $w_s = 0.1 \text{ m s}^{-1}$, which is within the range of values that have been reported for fresh snow particles [e.g. Kajikawa, 1972; Lehning et al., 2008]. While particle deposition patterns are expected to be a function of the Stokes number St_H , an exploration of the full parameter space is beyond the scope of the present article.

4.2. Results

In this section we present results of large eddy simulations of snow deposition onto surface topography. In Sec. 4.2.1, we will consider the mass conservation of the proposed model; instantaneous and time-average snap-

Table 2. Simulation properties for snow deposition case study.

Quantity	Symbol	Value
Domain [m]	$L_x \times L_y \times L_z$	$640 \times 320 \times 96$
Number of gridpoints [-]	$N_x \times N_y \times N_z$	$128 \times 64 \times 96$
Grid spacing [m]	$\Delta x \times \Delta y \times \Delta z$	$5 \times 5 \times 1$
Timestep [s]	Δt	0.025
Friction velocity [m s^{-1}]	u_*	0.20
Characteristic timescale [s]	$T_\ell = L_z/u_*$	473
Duration of particle release [-]	nT_ℓ	$n = 7.6$
Roughness length [m]	z_0	0.01
Settling velocity [m s^{-1}]	w_s	0.10
SGS Schmidt number [-]	Sc_{sgs}	1.0
Release rate [kg s^{-1}]	Q_{src}	145.
Source height [m]	z_{src}	95
Hill height [m]	H	20
Hill length [m]	L	40
Hill centerline [m]	x_0	80
Stokes number [-]	$St_H = \tau_p u_* / H$	1.0×10^{-4}

shots of the flow will be presented in Sec. 4.2.2. Deposition patterns will be discussed in Sec. 4.2.3, and the connection between flow acceleration, particle inertia,

and the observed deposition patterns will be explored in Sec. 4.2.4.

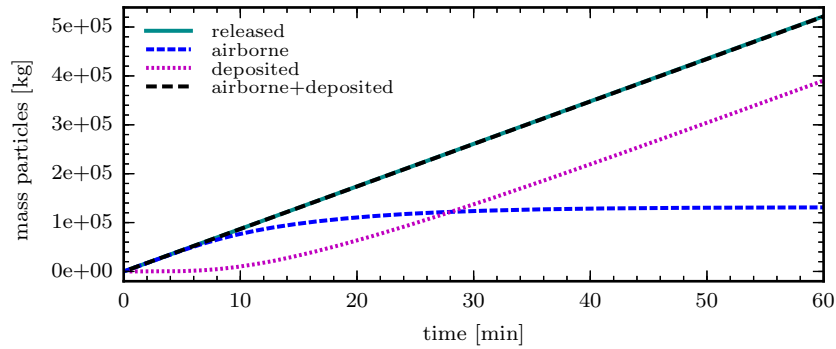


Figure 4. Mass balance of 1 hour particle release over surface topography, including total mass of particles released, airborne, deposited, and the sum of airborne + deposited.

4.2.1. Mass Conservation

As discussed earlier in Sec. 2.4, the motivation for developing a Cartesian cut cell method is to explicitly enforce mass conservation in the particle phase. In Fig. 4, we present the global mass balance for a 1 hour particle release over surface topography. Separate curves indicate the mass of particles released, airborne, and deposited, and the sum of airborne + deposited, which should match the release rate if mass conservation is accurate. Here one can see that the global mass balance reaches equilibrium after a time of approximately $L_z/w_s \sim 960$ s (or 16 minutes), which is approximately the time it takes for the first particles released to begin depositing on the surface. After this, the mass of particles airborne and the deposition rate are both constant. Note that the mass of particles airborne + deposited is very close to the total mass released. After

a 1 hour particle release, the residual of the mass balance (i.e. (released – airborne – deposited)/released) is within 0.10%, which demonstrates that the proposed numerical model does indeed conserve mass accurately.

It must be emphasized that accurate mass conservation is essential for physically realistic simulations of the transport of heavy particles or passive scalars over complex terrain. In order to ensure mass conservation, the treatment at the interface is of central importance; spurious fluxes induced by truncation errors or non-conservative treatment of quantities at the fluid-solid interface can deteriorate the quality of both local and global statistics. As discussed by *Mittal and Iaccarino* [2005], local and global mass conservation in the presence of an immersed boundary can only be guaranteed in a finite-volume framework, as we employ in the Cartesian cut cell method developed here.

4.2.2. Velocity and concentration fields

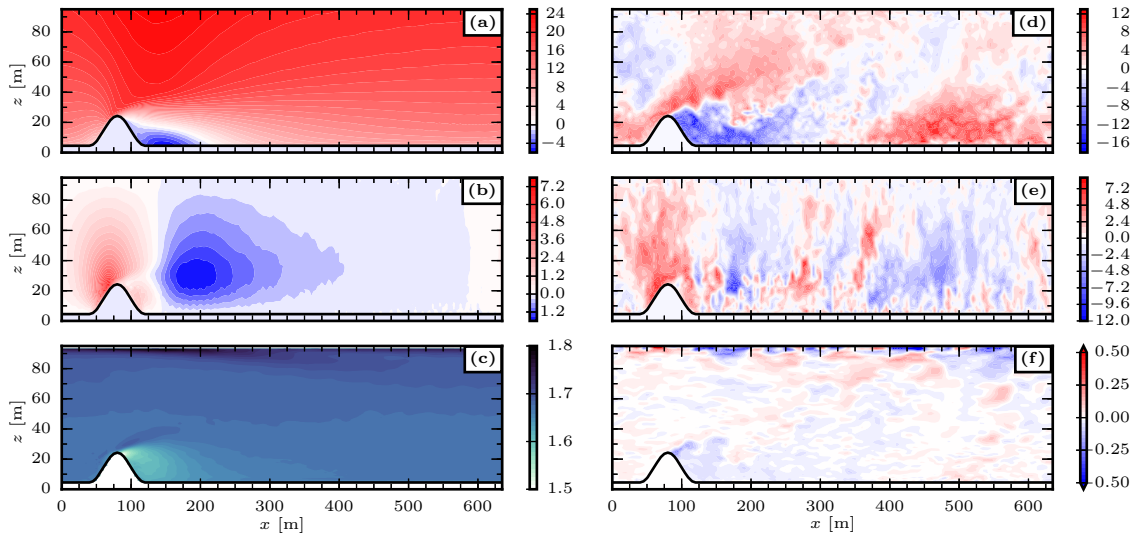


Figure 5. Visualization of velocity and particle concentration from LES. Time averaged quantities are displayed in panels (a)–(c) and instantaneous fluctuating quantities (with the horizontal mean removed) at $y = Ly/2$ are displayed in panels (d)–(f). (a) Average streamwise velocity U/u_* (b) average vertical velocity W/u_* (c) average particle concentration C/c_* (d) fluctuating streamwise velocity u'/u_* (e) fluctuating vertical velocity w'/u_* (f) fluctuating particle concentration c'/c_* .

A visualization of the instantaneous and averaged velocity and concentration fields can be found in Fig. 5. Here we use the Reynolds averaging convention, where a total resolved variable from the LES is decomposed into its mean and fluctuating parts, e.g. $\tilde{u} = U + u'$. Fluctuating quantities are calculated by removing the mean value calculated by averaging in the fluid only.

Although this flow cannot be considered horizontally homogeneous due to the presence of topography, we do this because our focus is on how topography modifies quantities from their values found in the corresponding case over statistically homogeneous, flat terrain. For simplicity of notation, we shall also omit the tilde ($\tilde{\cdot}$) from filtered variables, unless necessary. Variables are normalized using the friction velocity $u_* = \sqrt{-\tau_w/\rho} =$

$(\overline{u'w'^2})^{1/4}$ and the concentration scale $c_* = |\overline{w'c'_0}|/u_*$, where $|\overline{w'c'_0}|$ is the magnitude of the surface concentration flux. The velocity and concentration scales u_* and c_* are calculated by averaging just outside immersed boundary interface (i.e. in the region $0 \leq \varphi \leq \Delta z$); mean values of concentration, velocity, turbulent fluxes, etc. displayed in Figs. 5–8 are calculated by averaging in time and in the y -direction.

One can see from Fig. 5(a)–(b) that for this particular hill geometry, the flow detaches in the wake of the hill and a separation bubble forms such that $U/u_* < 0$. (Note that flow separation over smooth two-dimensional ridges is expected to occur for hill slopes of $\theta \gtrsim 18^\circ$, where θ decreases with increasing surface roughness [Kaimal and Finnigan, 1994]). The reattachment point is slightly more than $2L$ from the end of the hill on the leeward side. Due to the topography, there is also a region of positive average vertical velocity ($W > 0$) on the windward side of the hill, and average negative vertical velocity ($W < 0$) on the leeward side. A region of low particle concentration is found in the wake of the hill, and extends slightly beyond the reattachment point. In addition, a “streamer” of high concentration extends beyond the hill crest. Similar patterns are visible in the instantaneous velocity and concentration fields, displayed in Fig. 5(d)–(f).

4.2.3. Deposition Patterns

A plot of the average concentration field in the x - z plane with velocity vectors overlaid can be found in Fig. 6(a); in panel (b) we show a plot of deposition patterns from the LES after a 1-hour particle release. Panel (c) contains a figure of the y -averaged deposition after the conclusion of the particle release. Note that the dashed lines in panels (b)–(c) correspond to the edges and crest of the sinusoidal hill. We find that the deposition from the LES increases on the windward side of the hill, decreases sharply on the leeward side, and reaches a quasi-constant value in the far wake, as

seen in panel (c). The maximum value of deposition (approximately 4–5% larger than the upwind value) is found on the windward side of the hill, slightly before the crest; the minimum occurs on the leeward side just beyond the crest and is $\sim 9\%$ lower than the upwind value. This deposition pattern is qualitatively similar to previous observational and laboratory studies of particle deposition onto topography [e.g. Goossens, 2006]. The deposition patterns can be seen more clearly in the planview, plotted in Fig. 6(b). Note that, although the topography and the flow can be considered to be homogeneous in the y -direction, some lateral variability in the mass of particles deposited does occur downwind of the hill (e.g. around $x = 200$ to 600 m). We found from simulations of particle deposition onto a flat surface (not shown) with the same grid and domain that particle deposition varies spatially by no more than $\pm 1\%$ when no topography is present. When topography is present, deposition varies in the spanwise direction by $\sim 8\%$ in the wake of the hill; this is due to long-lived high- and low- speed streaks in the streamwise velocity field.

Average contours of the particle concentration field with velocity vectors overlaid can be found in Fig. 6(a). Here one can see that the region of high particle concentration immediately upwind of the hill is responsible for the enhanced deposition on the windward side of the hill; likewise, the low deposition in the wake is due to the lower particle concentrations. From Fig. 6 one can see that the y -averaged deposition does not vary significantly in the streamwise direction after about $x = 300$ m; this is where C becomes quasi-constant in the streamwise direction and occurs approximately 80 m after the reattachment point. Note, however, that the reattachment point and the location where C recovers to a quasi-constant value do not coincide due to particle inertia, which leads to relative velocities between the particles and fluid, which will be discussed more below.

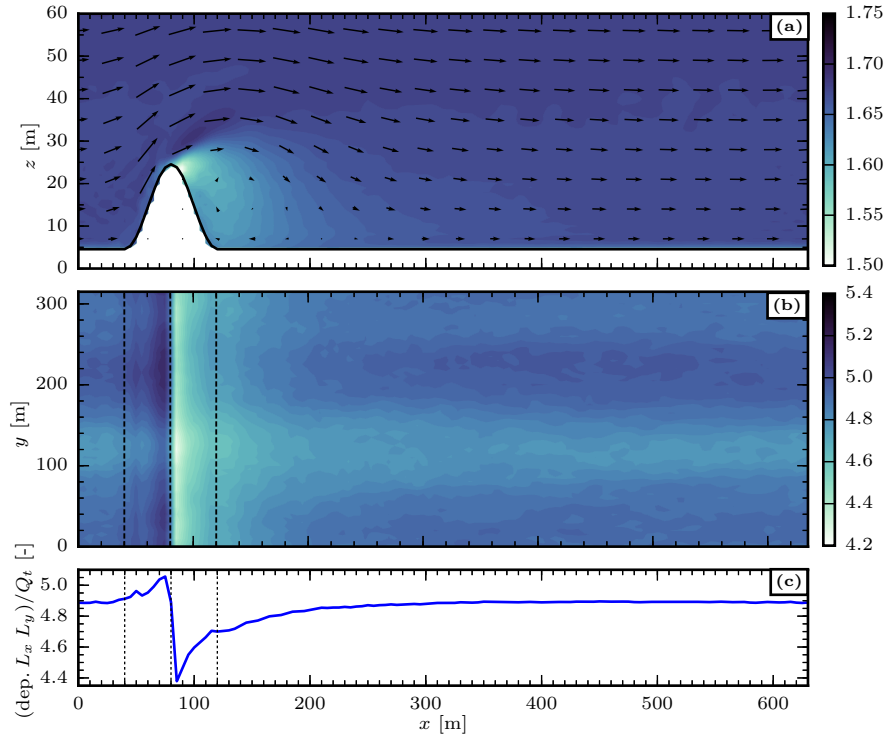


Figure 6. Average velocity and particle concentration and deposition from area source release over two-dimensional hill. (a) Contours of average particle concentration C/c_* in x - z plane with velocity vectors overlaid (b) nondimensional deposition, i.e. $(\text{deposition} \times L_x \times L_y) / Q_t$, in x - y plane after 1 hour particle release (c) nondimensional y -averaged deposition as a function of x .

4.2.4. Particle Inertia and Acceleration

The region of increased particle concentration beginning on the windward side of the hill and extending beyond the crest and the subsequent increase in deposition can be understood by noting that heavy particles will not follow the fluid flow field exactly due to their inertia. This “preferential concentration” effect is well-known in

the multiphase flow literature [e.g. *Squires and Eaton*, 1991; *Wang and Maxey*, 1993; *Eaton and Fessler*, 1994]; the extent to which it occurs is a function of the Stokes number. However, many of these studies focused on preferential concentration in homogeneous isotropic turbulence. We here consider the effects of particle inertia on the concentration field in wall-bounded turbulent shear flows over complex topography and the implications for particle deposition.

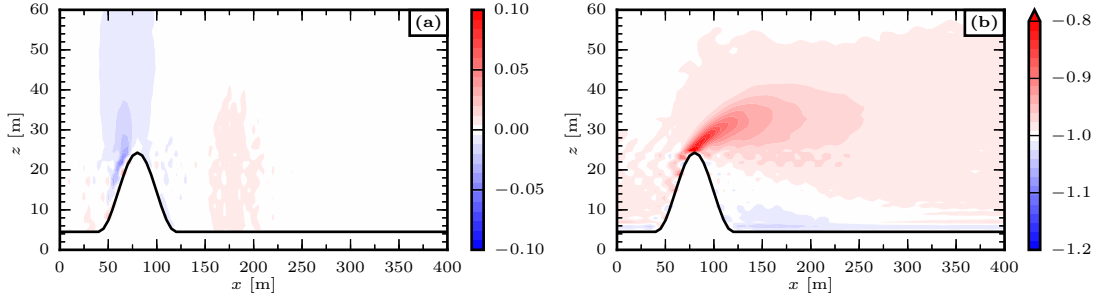


Figure 7. Relative velocity between particles and fluid $\mathbf{v}^{rel} = \tilde{\mathbf{v}}_p - \tilde{\mathbf{u}} = \tau_p \mathbf{g} - \tau_p \tilde{\mathbf{a}}$, normalized by the background settling velocity w_s . (a) x -component of relative velocity, $v_x^{rel}/w_s = -\tau_p a_x/w_s$ (b) z -component of relative velocity, $v_z^{rel}/w_s = -(\tau_p a_z + w_s)/w_s$.

From the expression for the particle advection velocity (8), one can write the relative velocity between the particles and fluid as:

$$\tilde{\mathbf{v}}_{rel} = \tilde{\mathbf{v}}_p - \tilde{\mathbf{u}} = \tau_p \mathbf{g} - \tau_p \tilde{\mathbf{a}}, \quad (28)$$

demonstrating that relative velocities between the particles and fluid occur due to a combination of gravitational settling and particle inertia.

The time- and laterally-averaged x - and z -components of relative velocity are plotted in Fig. 7 in panels (a) and (b), respectively. One can see that the x -component of relative velocity is negative on the windward side of the hill due to the positive streamwise acceleration $a_x > 0$ in this region. Here particles cross fluid streamlines, leading to the “streamer” of high concentration observed in Fig. 6(a) and the subsequent increase in deposition on the windward side of the hill. In this region, v_x^{rel} is negative, and has a magnitude of ~ 5 -6% of w_s . A region of positive v_x^{rel} is found in the wake of the hill where the flow decelerates. Here the magnitude of v_x^{rel} is ~ 4 -5% of w_s . In Fig. 7(b), one can see that far away from the hill, the z -component of relative velocity is due strictly to the constant gravitational settling velocity. However, downstream and above the crest of the hill, the vertical component of relative velocity is reduced; here v_z^{rel} is as small as $\sim 80\%$ of w_s . This region corresponds to where low concentration is found in the wake, as once can see in Fig. 5, where deposition is at its minimum.

When *Lehning et al.* [2008] introduced the concept of preferential deposition of snow in mountains, they suggested that more snow may be deposited in the lee of a steep alpine ridge. The study of *Mott and Lehning* [2010] obtained similar results for the same ridge, while *Mott et al.* [2010] found more preferential deposi-

tion on the windward side of steep slopes for a different experimental area (their Fig. 14a). Our results clearly suggest that lee slopes may receive a minimum of precipitation. This is in partial contradiction to the earlier “simple ridge” cases. The combination of Advanced Regional Prediction System (ARPS) RANS wind simulations with Alpine3D deposition modeling as applied in all three previous investigations does not properly account for particle inertia, which may explain some of the differences. On the other hand, *Mott et al.* [2014] have recently shown that higher concentrations are often found downwind of ridges, at least higher up in the atmosphere. Further studies are therefore required to determine the dependence of preferential deposition patterns on the wind fields and topography (which can be expressed in terms of the Stokes number St_H) as well as other factors (e.g. atmospheric stability). The results for the relative velocities and deposition patterns presented here therefore should not be taken as general; a more comprehensive investigation of the dependence of preferential deposition on St_H and other parameters will be addressed in future work.

In order to investigate the role of mean vs. fluctuating inertia for the preferential concentration of particles, one can Reynolds average the inertia terms that appear in the particle conservation equation (5), i.e.

$$\overline{\tau_p \tilde{\mathbf{a}} \cdot \nabla \tilde{C}} = \tau_p \left(\overline{\bar{a}_x \frac{\partial \tilde{C}}{\partial x}} + \overline{\bar{a}_z \frac{\partial \tilde{C}}{\partial z}} + \overline{a'_x \frac{\partial \tilde{c}'}{\partial x}} + \overline{a'_z \frac{\partial \tilde{c}'}{\partial z}} \right) \quad (29)$$

Here the y derivatives are neglected due to lateral homogeneity. The average mean and turbulent x - and z - inertia terms are displayed in Fig. 8, where all terms have been nondimensionalized by u_* , c_* , and L_z . One can see in panels (a)–(b) that the mean streamwise inertia leads to the increase concentration of par-

ticles on the windward side of the hill. In contrast, the turbulent component of streamwise inertia is quite small. The mean z -component also contributes to the increased particle concentration on the windward side of the hill, as well as to the “streamer” of high concentration that extends beyond the crest. Note here that the contours for the z -component are a factor of 5 larger than those for the x -component. The turbulent z -inertia component is at its maximum downwind of the hill at and slightly above hill height, but is smaller than the mean z -component. In contrast to previous studies

of preferential concentration in homogeneous, isotropic turbulence, flows over surface topography have regions of strong mean accelerations. We find here that for the simulation considered here, mean inertia dominates over the turbulent contribution; in fact, the mean component of z -inertia is 6-7 times larger than the turbulent component. This observation is an important detail for future developments in models of particle deposition in complex terrain, where the enhancement of deposition can potentially be modeled in terms of mean flow quantities (e.g. mean concentration and acceleration).

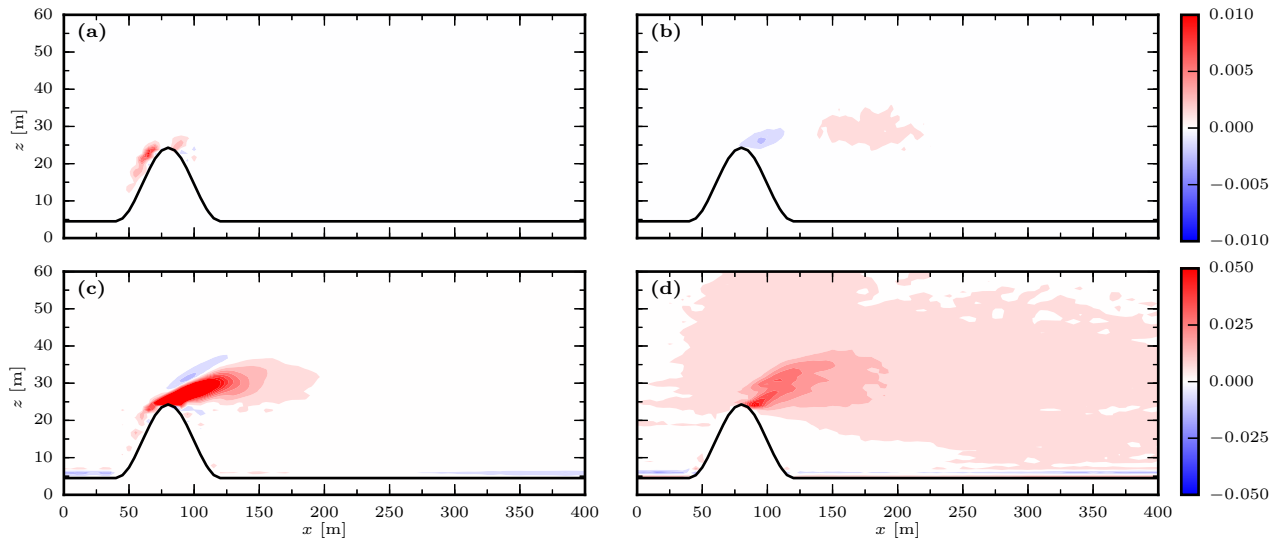


Figure 8. Mean and turbulent inertia terms in particle equation, averaged in time and lateral direction.

- (a) Mean component of x -inertia term, $\frac{L_z}{c_* u_*} \bar{a}_x \frac{\partial \bar{C}}{\partial x}$ (b) turbulent component of x -inertia term, $\frac{L_z}{c_* u_*} a'_x \frac{\partial c'}{\partial x}$,
(c) Mean component of z -inertia term, $\frac{L_z}{c_* u_*} \bar{a}_z \frac{\partial \bar{C}}{\partial z}$ (d) turbulent component of z -inertia term, $\frac{L_z}{c_* u_*} a'_z \frac{\partial c'}{\partial z}$

5. Discussion and Conclusions

A new approach for modeling the transport and deposition of heavy particles over complex surface topography was developed using the large eddy simulation technique. An immersed boundary LES code (using the discrete direct forcing approach) was coupled with an Eulerian finite-volume particle code. The advection-diffusion equation for particle mass conservation was discretized using a Cartesian cut cell method that reshapes finite volume cells intersected by the zero level set (i.e. the fluid-solid interface). Small cells (with volume fraction $\alpha < 0.5$) are treated using the conservative mixing model of *Meyer et al.* [2010] which alleviates the

restrictive local CFL requirements. In order to obtain a divergence-free interpolated velocity field on finite volume faces intersected by the zero level set, we use a projection-type method, by first calculating an intermediate interpolated velocity (with finite divergence) following the approach of *Chamecki et al.* [2008], then solving a Poisson equation to obtain a divergence-free interpolated velocity. The proposed numerical method conserves mass accurately, i.e. within 0.1% for simulations of snow deposition over idealized topography. Accurate mass conservation is essential when simulating the transport of heavy particles and passive scalars over complex terrain or in urban environments, motivating our development of a Cartesian cut-cell finite volume method.

The proposed numerical model was validated by comparing simulation results with the wind tunnel study of *Goossens* [2006], who conducted wind tunnel experiments of heavy particle deposition over idealized topography. At fine ($128 \times 64 \times 96$) resolution, the LES results were found to be in reasonably good agreement with observed deposition patterns, although we find that the results are SGS model-dependent. In particular, the Lagrangian scale-dependent dynamic model [*Bou-Zeid et al.*, 2005] is found to overpredict deposition on the windward side of an obstacle. This is likely related to the fact that the test filters at scale 2Δ and 4Δ use points inside the immersed boundary (with nonphysical velocities) to determine a value of the Smagorinsky coefficient c_s and therefore the SGS scalar diffusivity (in the present study we use a constant SGS Schmidt number model for the scalar concentration field). In principle, one could modify the filtering operation so that only points in the fluid are included in the stencil of the test filters. Although dynamic SGS models for scalars exist [e.g. *Stoll and Porté-Agel*, 2006], these too would suffer from the same issue of filtering inside the IBM surface.

An idealized simulation of snow deposition over a two-dimensional sinusoidal hill revealed that deposition reached its maximum on the windward side of a hill, and its minimum on the leeward side, consistent with previous studies of aeolian processes [e.g. *Goossens*, 2006]. The enhanced deposition on the windward side of the hill can be explained by noting that particle inertia leads to relative velocities between the particles and fluid, thereby enhancing concentration on the windward side of the hill. On the leeward side of the hill, inertia leads to a decreased settling velocity and lower particle deposition. Reynolds averaging revealed that, for our simulation, the mean inertia terms in the particle mass conservation equation are larger than their turbulent counterparts by a factor of 6 or more.

Our current results and previous studies [*Lehning et al.*, 2008; *Mott and Lehning*, 2010; *Mott et al.*, 2010, 2014] demonstrate that preferential deposition patterns depend on topographic features, and wind fields as well as other factors such as atmospheric stratification. We find from our present results that particle inertia is also significant for determining the spatial variability of the deposition of heavy particles in complex terrain. Our results indicate that Eulerian models of heavy particle transport in complex terrain should include a model to account for the effects of particle inertia [e.g. *Shotorban and Balachandar*, 2007; *Balachandar and Eaton*, 2010] in order to recover physically realistic deposition patterns. When inertia is excluded, the simulations fail to recover deposition patterns in quantitative or qualitative agreement with experimental data.

While erosion is not addressed in this work, snow or sediment transport over topography will also be influenced by erosion when the friction velocity u_* exceeds

the threshold value u_{*t} , thereby initiating saltation [e.g. *Bagnold*, 1941]. Implementing a model for saltation and investigating the combined impacts of erosion and deposition will be considered in future work.

The proposed numerical model conserves mass accurately, is computationally inexpensive, and is well suited for investigating a variety of problems, including snow and sediment transport, the dispersal of biogenic particles, and scalar dispersion in urban environments and complex terrain.

Acknowledgments. MBP gratefully acknowledges support from the National Sciences and Engineering Research Council of Canada (NSERC) under the Discovery Grants program. The authors thank Elie Bou-Zeid for helpful suggestions. Simulations were run on the Mammouth Parallèle 2 cluster at the Université de Sherbrooke and the Guillimin cluster at McGill University, managed by Calcul Québec and Compute Canada. The operation of these supercomputers is funded by the Canadian Foundation for Innovation (CFI), Ministère de l'Économie, de l'Innovation et des Exportations du Québec (MEIE), RMGA and the Fonds de Recherche du Québec - Nature et Technologies (FRQ-NT). Data from the large eddy simulations used in this study are available upon request from the corresponding author (STS, salesky@ou.edu).

Appendix A: Cut Cell Geometry

All of the geometric quantities needed for the Cartesian cut cell method (area fractions of the cut faces, volume fraction of a cell in the fluid, and the area of a cut face) can be calculated from the level set function φ . In order to calculate the area fraction of a cut face, the level set function is first interpolated to the vertices of that face using trilinear interpolation (note that φ is stored on the w nodes). An example of a z -face intersected by the IBM surface with two of these intersection points, (x_2, y_2) and (x_3, y_3) , where $\varphi = 0$, can be found in Fig. 9.

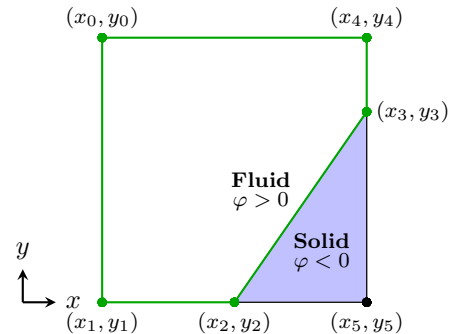


Figure 9. A schematic diagram of intersection points on the z -face of a cut cell, used to calculate the area fraction of face in the fluid.

In order to locate the intersection points, φ is first interpolated to the four vertices of a cut face. Faces intersected by the zero level set are identified where φ changes sign between the two adjoining vertices. For example, the x -coordinate of the intersection point on

the bottom y -face in Fig. 2 (i.e. x_2) would be located by

$$x_2 = \frac{x_{sw}\varphi_{se} - x_{se}\varphi_{sw}}{\varphi_{se} - \varphi_{sw}} \quad (\text{A1})$$

where $x_{sw} = x_1 = 0$ and $x_{se} = x_5 = \Delta x$, $\varphi_{sw} = \varphi(x_1, y_1)$, and $\varphi_{se} = \varphi(x_5, y_5)$.

Once the intersection points are located, the area of the face in the fluid can be calculated using Green's theorem, e.g. for a z -face,

$$S^z = A^z \Delta x \Delta y = \sum_{k=0}^n \frac{1}{2} (x_{k+1} + x_k)(y_{k+1} - y_k) \quad (\text{A2})$$

where the sum is taken over the n vertices of the polygon that surround the part of the face in the fluid. For the z -face depicted in Fig. 9, one would sum over the vertices $(x_0, y_0), \dots, (x_4, y_4)$ to calculate the area of the region outlined in green.

The area of the cut face (S^Γ) can be calculated using de Gua's theorem (an analogue of the Pythagorean theorem for right tetrahedra):

$$S_{i,j,k}^\Gamma = [(S_{i+1/2}^x - S_{i-1/2}^x)^2 + (S_{j+1/2}^y - S_{j-1/2}^y)^2 + (S_{k+1/2}^z - S_{k-1/2}^z)^2]^{1/2}, \quad (\text{A3})$$

and the normal vector on the cut face can be calculated via:

$$\mathbf{n}_{i,j,k}^\Gamma = \frac{1}{S^\Gamma} \begin{pmatrix} S_{i+1/2}^x - S_{i-1/2}^x \\ S_{j+1/2}^y - S_{j-1/2}^y \\ S_{k+1/2}^z - S_{k-1/2}^z \end{pmatrix} \quad (\text{A4})$$

Once the face areas have been calculated, the volume fraction of a cut cell can be calculated using the divergence theorem:

$$\alpha_{i,j,k} = \frac{1}{\Delta x \Delta y \Delta z} \sum_{\ell} \frac{1}{3} (\mathbf{x}_\ell \cdot \mathbf{n}_\ell S_\ell + \mathbf{x}_\Gamma \cdot \mathbf{n}_\Gamma S_\Gamma) \quad (\text{A5})$$

where \mathbf{x}_ℓ , \mathbf{n}_ℓ , and S_ℓ are respectively a point on the ℓ th face, the outward facing normal vector on that face, and the face area; \mathbf{x}_Γ , \mathbf{n}_Γ , and S_Γ represent the corresponding quantities on the cut face (e.g. the sum would be taken over regular faces $\ell = 1, \dots, 6$ and the cut face for the finite volume cell depicted in Fig. 2). For the case of a fixed surface height as in the present work (i.e. where the level set is not advected), all geometric quantities are calculated once at the beginning of the computation and stored.

Appendix B: Conservative Mixing Model

In the finite volume Cartesian cut cell code, we employ the conservative mixing model of Meyer *et al.* [2010] to address the so-called ‘‘small cell problem’’ to circumvent the need to decrease the timestep in cut cells with small volume fractions in order to satisfy the local CFL condition. The mixing procedure is performed each timestep after AB2 time advancement, and is summarized here briefly. The concentration exchanged between a small cell (i, j, k) and a target cell in the positive

x -direction $(i + 1, j, k)$, is given as:

$$X^x = \frac{\beta_{i,j,k}^x \mathcal{V}_{i,j,k} \mathcal{V}_{i+1,j,k}}{\beta_{i,j,k}^x \mathcal{V}_{i,j,k} + \mathcal{V}_{i+1,j,k}} [\tilde{C}_{i+1,j,k} - \tilde{C}_{i,j,k}] \quad (\text{B1})$$

where $\mathcal{V}_{i,j,k} = \Delta x \Delta y \Delta z \alpha_{i,j,k}$ is the volume of cell (i, j, k) and $\beta_{i,j,k}^x$ is a mixing fraction, defined below. Similar terms are calculated for the other neighboring cells; a small cell will mix concentration with seven neighboring cells in 3D. The mixing fractions are given as

$$\begin{aligned} \beta_{i,j,k}^x &= |n_x^\Gamma n_x^\Gamma| (\alpha_{target}^x)^\mu \\ \beta_{i,j,k}^y &= |n_y^\Gamma n_y^\Gamma| (\alpha_{target}^y)^\mu \\ \beta_{i,j,k}^z &= |n_z^\Gamma n_z^\Gamma| (\alpha_{target}^z)^\mu \\ \beta_{i,j,k}^{xy} &= |n_x^\Gamma n_y^\Gamma| (\alpha_{target}^{xy})^\mu \\ \beta_{i,j,k}^{xz} &= |n_x^\Gamma n_z^\Gamma| (\alpha_{target}^{xz})^\mu \\ \beta_{i,j,k}^{yz} &= |n_y^\Gamma n_z^\Gamma| (\alpha_{target}^{yz})^\mu \\ \beta_{i,j,k}^{xyz} &= |n_x^\Gamma n_y^\Gamma n_z^\Gamma|^{2/3} (\alpha_{target}^{xyz})^\mu \end{aligned} \quad (\text{B2})$$

where $\mathbf{n}^\Gamma = (n_x^\Gamma, n_y^\Gamma, n_z^\Gamma)$ is the normal vector on the cut face, α_{target} is the volume fraction of the ‘‘target cell’’ for mixing and is determined by the direction of the normal vector, i.e.

$$\alpha_{target}^x = \begin{cases} \alpha_{i+1,j,k}, & n_x^\Gamma > 1 \\ \alpha_{i-1,j,k}, & n_x^\Gamma < 1 \end{cases}, \quad (\text{B3})$$

and $\mu \geq 1$ is an integer to give a larger weight to cells with large volume fractions for the sake of numerical stability. Meyer *et al.* [2010] used a value of $\mu = 5$; we find little sensitivity to the value of μ employed. Note that the mixing fractions normalize to 1, i.e.

$$\beta_{i,j,k}^x + \beta_{i,j,k}^y + \beta_{i,j,k}^z + \beta_{i,j,k}^{xy} + \beta_{i,j,k}^{xz} + \beta_{i,j,k}^{yz} + \beta_{i,j,k}^{xyz} = 1 \quad (\text{B4})$$

After calculating the mixing fractions and exchanging concentrations, the concentration in the small cells and target cells are updated, e.g. in a target cell via

$$\tilde{C}_{i+1,j,k} = \tilde{C}_{i+1,j,k}^* - \frac{1}{\mathcal{V}_{i+1,j,k}} X^x \quad (\text{B5})$$

and in the small cell by

$$\tilde{C}_{i,j,k} = \tilde{C}_{i,j,k}^* + \frac{1}{\mathcal{V}_{i,j,k}} [X^x + X^y + X^z + X^{xy} + X^{xz} + X^{yz} + X^{xyz}] \quad (\text{B6})$$

where $\tilde{C}_{i,j,k}^*$ is the value of concentration before conservative mixing.

References

- Albertson, J. D., and M. B. Parlange (1999), Surface length scales and shear stress: Implications for land-atmosphere interaction over complex terrain, *Water Resour. Res.*, *35*(7), 2121–2132.
- Aylor, D. E. (1982), Modeling spore dispersal in a barley crop, *Ag. Meteorol.*, *26*(3), 215–219.
- Aylor, D. E. (1990), The role of intermittent wind in the dispersal of fungal pathogens, *Ann. Rev. Phytopathol.*, *28*(1), 73–92.

- Aylor, D. E. (2002), Settling speed of corn (*Zea mays*) pollen, *J. Aerosol Sci.*, *33*(11), 1601–1607.
- Aylor, D. E., and J.-Y. Parlange (1975), Ventilation required to entrain small particles from leaves, *Plant Physiol.*, *56*(1), 97–99.
- Aylor, D. E., J.-Y. Parlange, and J. Granett (1976), Turbulent dispersion of disparlure in the forest and male gypsy moth response, *Environ. Entomol.*, *5*(5), 1026–1032.
- Aylor, D. E., N. P. Schultes, and E. J. Shields (2003), An aerobiological framework for assessing cross-pollination in maize, *Ag. Forest Meteorol.*, *119*(3), 111–129.
- Bagnold, R. (1941), *The physics of blown sand and desert dunes*, London: Methuen, 265 pp.
- Balachandar, S., and J. K. Eaton (2010), Turbulent dispersed multiphase flow, *Ann. Rev. Fluid Mech.*, *42*, 111–133.
- Balk, B., and K. Elder (2000), Combining binary decision tree and geostatistical methods to estimate snow distribution in a mountain watershed, *Water Resour. Res.*, *36*(1), 13–26, doi:10.1029/1999WR900251.
- Best, J. (2005), The fluid dynamics of river dunes: A review and some future research directions, *J. Geophys. Res.*, *110*(F4).
- Blöschl, G., and R. Kirnbauer (1992), An analysis of snow cover patterns in a small alpine catchment, *Hydrol. Proc.*, *6*, 99–109.
- Bou-Zeid, E., C. Meneveau, and M. Parlange (2005), A scale-dependent Lagrangian dynamic model for large eddy simulation of complex turbulent flows, *Phys. Fluids*, *17*(2), 025,105.
- Bowman, W. D. (1992), Inputs and storage of nitrogen in winter snowpack in an alpine ecosystem, *Arctic Alpine Res.*, pp. 211–215.
- Briaud, J.-L., F. C. Ting, H. Chen, R. Gudavalli, S. Perugu, and G. Wei (1999), SRICOS: Prediction of scour rate in cohesive soils at bridge piers, *J. Geotech. Geoenviron.*, *125*(4), 237–246.
- Brown, J. K., and M. S. Hovmöller (2002), Aerial dispersal of pathogens on the global and continental scales and its impact on plant disease, *Science*, *297*(5581), 537–541.
- Cain, M. L., B. G. Milligan, and A. E. Strand (2000), Long-distance seed dispersal in plant populations, *Am. J. Bot.*, *87*(9), 1217–1227.
- Canuto, C., M. Y. Hussaini, A. M. Quarteroni, A. Thomas Jr, et al. (2012), *Spectral methods in fluid dynamics*, Springer Science & Business Media, 539 pp.
- Cermak, J. (1984), Physical modelling of flow and dispersion over complex terrain, *Bound.-Layer Meteorol.*, *30*(1), 261–292.
- Chamberlain, A. (1967), Transport of Lycopodium spores and other small particles to rough surfaces, in *Proc. Roy. Soc. A*, vol. 296, pp. 45–70, The Royal Society.
- Chamecki, M. (2012), An analytical model for dispersion of biological particles emitted from area sources: Inclusion of dispersion in the crosswind direction, *Ag. Forest Meteorol.*, *157*, 30–38.
- Chamecki, M., and C. Meneveau (2011), Particle boundary layer above and downstream of an area source: scaling, simulations, and pollen transport, *J. Fluid Mech.*, *683*, 1–26.
- Chamecki, M., C. Meneveau, and M. B. Parlange (2008), A hybrid spectral/finite-volume algorithm for large-eddy simulation of scalars in the atmospheric boundary layer, *Bound.-Layer Meteorol.*, *128*(3), 473–484.
- Chamecki, M., C. Meneveau, and M. B. Parlange (2009), Large eddy simulation of pollen transport in the atmospheric boundary layer, *J. Aerosol Sci.*, *40*(3), 241–255.
- Charru, F., B. Andreotti, and P. Claudin (2013), Sand ripples and dunes, *Ann. Rev. Fluid Mech.*, *45*, 469–493.
- Chen, B., D. Yang, C. Meneveau, and M. Chamecki (2016), Effects of swell on transport and dispersion of oil plumes within the ocean mixed layer, *J. Geophys. Res.*, *121*(5), 3564–3578, doi:10.1002/2015JC011380.
- Chester, S., C. Meneveau, and M. B. Parlange (2007), Modeling turbulent flow over fractal trees with renormalized numerical simulation, *J. Comp. Phys.*, *225*(1), 427–448.
- Chorin, A. J. (1968), Numerical solution of the Navier-Stokes equations, *Math. Computation*, *22*(104), 745–762.
- Chou, Y.-J., and O. B. Fringer (2008), Modeling dilute sediment suspension using large-eddy simulation with a dynamic mixed model, *Phys. Fluids*, *20*(11), 115,103.
- Das, I., R. E. Bell, T. A. Scambos, M. Wolovick, T. T. Creyts, M. Studinger, N. Frearson, J. P. Nicolas, J. T. Lenaerts, and M. R. van den Broeke (2013), Influence of persistent wind scour on the surface mass balance of Antarctica, *Nat. Geosci.*, *6*(5), 367–371.
- Das, I., T. A. Scambos, L. S. Koenig, M. R. Broeke, and J. Lenaerts (2015), Extreme wind-ice interaction over Recovery Ice Stream, East Antarctica, *Geophys. Res. Lett.*, *42*(19), 8064–8071.
- Demuren, A. O., and W. Rodi (1986), Calculation of flow and pollutant dispersion in meandering channels, *J. Fluid Mech.*, *172*, 63–92.
- Déry, S. J., A. Clifton, S. MacLeod, and M. J. Beedle (2010), Blowing snow fluxes in the Cariboo mountains of British Columbia, Canada, *Arc. Antarct. Alp. Res.*, *42*(2), 188–197.
- Di-Giovanni, F., and P. Kevan (1991), Factors affecting pollen dynamics and its importance to pollen contamination: a review, *Can. J. Forest Res.*, *21*(8), 1155–1170.
- Dupont, S., Y. Brunet, and N. Jarosz (2006), Eulerian modelling of pollen dispersal over heterogeneous vegetation canopies, *Ag. Forest Meteorol.*, *141*(2), 82–104.
- Dupont, S., G. Bergametti, B. Marticorena, and S. Simoëns (2013), Modeling saltation intermittency, *J. Geophys. Res.*, *118*(13), 7109–7128.
- Eaton, J. K., and J. Fessler (1994), Preferential concentration of particles by turbulence, *Int. J. Multiphase Flow*, *20*, 169–209.
- Eisen, O., M. Frezzotti, C. Genthon, E. Isaksson, O. Magand, M. R. van den Broeke, D. A. Dixon, A. Ekaykin, P. Holmlund, T. Kameda, et al. (2008), Ground-based measurements of spatial and temporal variability of snow accumulation in East Antarctica, *Rev. Geophys.*, *46*(2).
- Elder, K., J. Dozier, and J. Michaelsen (1991), Snow accumulation and distribution in an alpine watershed, *Water Resour. Res.*, *27*(7), 1541–1552.
- Engelund, F., and J. Fredsoe (1982), Sediment ripples and dunes, *Ann. Rev. Fluid Mech.*, *14*(1), 13–37.
- Evans, B. M., D. A. Walker, C. S. Benson, E. A. Nordstrand, and G. W. Petersen (1989), Spatial interrelationships between terrain, snow distribution and vegetation patterns at an Arctic foothills site in Alaska, *Ecography*, *12*(3), 270–278.
- Finn, J. R., M. Li, and S. V. Apte (2016), Particle based modelling and simulation of natural sand dynamics in the wave bottom boundary layer, *J. Fluid Mech.*, *796*, 340–385, doi:10.1017/jfm.2016.246.
- Freire, L., M. Chamecki, and J. Gillies (2016), Flux-profile relationship for dust concentration in the stratified atmospheric surface layer, *Bound.-Layer Meteorol.*, pp. 1–19.
- Gaskell, P., and A. Lau (1988), Curvature-compensated convective transport: SMART, a new boundedness-preserving transport algorithm, *Int. J. Num. Meth. Fl.*, *8*(6), 617–641.
- Gauer, P. (2001), Numerical modeling of blowing and drifting snow in alpine terrain, *J. Glaciol.*, *47*(156), 97–110.
- Goossens, D. (2006), Aeolian deposition of dust over hills: the effect of dust grain size on the deposition pattern, *Earth Surf. Proc.*, *31*(6), 762–776.
- Hartmann, D., M. Meinke, and W. Schröder (2008), An adaptive multilevel multigrid formulation for cartesian hierarchical grid methods, *Computers & Fluids*, *37*(9), 1103–1125.
- Helbig, N., B. Vogel, H. Vogel, and F. Fiedler (2004), Numerical modelling of pollen dispersion on the regional scale, *Aerobiologia*, *20*(1), 3–19.
- Högström, U. (1988), Non-dimensional wind and temperature profiles in the atmospheric surface layer: A re-evaluation, *Bound.-Layer Meteorol.*, *42*, 55–78.
- Hu, X., B. Khoo, N. A. Adams, and F. Huang (2006), A conservative interface method for compressible flows, *J. Comp. Phys.*, *219*(2), 553–578.
- Ingram, D. M., D. M. Causon, and C. G. Mingham (2003), Developments in Cartesian cut cell methods, *Math. Comput. Simulat.*, *61*(3), 561–572.
- Jickells, T., Z. An, K. K. Andersen, A. Baker, G. Bergametti, N. Brooks, J. Cao, P. Boyd, R. Duce, K. Hunter, et al. (2005), Global iron connections between desert dust, ocean biogeochemistry, and climate, *Science*, *308*(5718), 67–71.
- Kaimal, J. C., and J. J. Finnigan (1994), *Atmospheric boundary layer flows: their structure and measurement*, Oxford University Press, 289 pp.
- Kajikawa, M. (1972), Measurement of falling velocity of individual snow crystals, *J. Meteor. Soc. Japan*, *50*, 577–583.
- Khosronejad, A., and F. Sotiropoulos (2014), Numerical simulation of sand waves in a turbulent open channel flow, *J. Fluid Mech.*, *753*, 150–216.

- Khosronejad, A., S. Kang, I. Borazjani, and F. Sotiropoulos (2011), Curvilinear immersed boundary method for simulating coupled flow and bed morphodynamic interactions due to sediment transport phenomena, *Adv. Water Res.*, *34*(7), 829–843.
- Khosronejad, A., S. Kang, and F. Sotiropoulos (2012), Experimental and computational investigation of local scour around bridge piers, *Adv. Water Res.*, *37*, 73–85.
- Kind, R. (1992), One-dimensional aeolian suspension above beds of loose particles: a new concentration-profile equation, *Atmos. Environ.*, *26*(5), 927–931.
- Kirkpatrick, M., S. Armfield, and J. Kent (2003), A representation of curved boundaries for the solution of the Navier–Stokes equations on a staggered three-dimensional cartesian grid, *J. Comp. Phys.*, *184*(1), 1–36.
- Kobayashi, D., N. Ishikawa, and F. Nishio (1988), Formation process and direction distribution of snow cornices, *Cold Reg. Sci. Tech.*, *15*(2), 131–136.
- Kok, J. F., E. J. Parteli, T. I. Michaels, and D. B. Karam (2012), The physics of wind-blown sand and dust, *Rep. Prog. Phys.*, *75*(10), 106,901.
- Kumar, V., J. Kleissl, C. Meneveau, and M. B. Parlange (2006), Large-eddy simulation of a diurnal cycle of the atmospheric boundary layer: Atmospheric stability and scaling issues, *Water Resour. Res.*, *42*(6).
- Lamb, D., and J. Verlinde (2011), *Physics and chemistry of clouds*, Cambridge University Press, 584 pp.
- Lehning, M., H. Löwe, M. Rysler, and N. Raderschall (2008), Inhomogeneous precipitation distribution and snow transport in steep terrain, *Water Resour. Res.*, *44*(7).
- Lilly, D. K. (1992), A proposed modification of the Germano subgrid-scale closure method, *Phys. Fluids*, *4*(3), 633–635.
- Liston, G. E., and M. Sturm (1998), A snow-transport model for complex terrain, *J. Glaciol.*, *44*(148), 498–516.
- Luce, C. H., D. G. Tarboton, and K. R. Cooley (1998), The influence of the spatial distribution of snow on basin-averaged snowmelt, *Hydrol. Proc.*, *12*(1011), 1671–1683.
- MacVicar, B., L. Parrott, and A. Roy (2006), A two-dimensional discrete particle model of gravel bed river systems, *J. Geophys. Res.*, *111*(F3).
- Mason, P. J. (1994), Large-eddy simulation: A critical review of the technique, *Quart. J. Roy. Meteorol. Soc.*, *120*(515), 1–26.
- May, K., and R. Clifford (1967), The impaction of aerosol particles on cylinders, spheres, ribbons and discs, *Ann. Occup. Hyg.*, *10*(2), 83–95.
- Meneveau, C., T. S. Lund, and W. H. Cabot (1996), A Lagrangian dynamic subgrid-scale model of turbulence, *J. Fluid Mech.*, *319*, 353–385.
- Meyer, M., A. Devesa, S. Hickel, X. Hu, and N. Adams (2010), A conservative immersed interface method for large-eddy simulation of incompressible flows, *J. Comp. Phys.*, *229*(18), 6300–6317.
- Miller, R., I. Tegen, and J. Perlwitz (2004), Surface radiative forcing by soil dust aerosols and the hydrologic cycle, *J. Geophys. Res.*, *109*(D4).
- Mittal, R., and G. Iaccarino (2005), Immersed boundary methods, *Ann. Rev. Fluid Mech.*, *37*, 239–261.
- Mohd-Yusof, J. (1997), Combined immersed-boundary/B-spline method for simulations of flow in complex geometries, *Annual Research Briefs (Center for Turbulence Research, NASA Ames and Stanford University)*, pp. 317–328.
- Moran, S. M., E. R. Pardyjak, and J. M. Veranth (2013), Understanding the role of grid turbulence in enhancing pm10 deposition: Scaling the stokes number with R_λ , *Phys. Fluids*, *25*(11), 115,103.
- Mott, R., and M. Lehning (2010), Meteorological modeling of very high-resolution wind fields and snow deposition for mountains, *J. Hydrometeorol.*, *11*(4), 934–949.
- Mott, R., M. Schirmer, M. Bavay, T. Grünewald, and M. Lehning (2010), Understanding snow-transport processes shaping the mountain snow-cover, *The Cryosphere*, *4*(4), 545–559.
- Mott, R., D. Scipion, M. Schneebeli, N. Dawes, A. Berne, and M. Lehning (2014), Orographic effects on snow deposition patterns in mountainous terrain, *J. Geophys. Res.*, *119*(3), 1419–1439.
- Nagata, N., T. Hosoda, T. Nakato, and Y. Muramoto (2005), Three-dimensional numerical model for flow and bed deformation around river hydraulic structures, *J. Hydraulic Eng.*, *131*(12), 1074–1087.
- Nathan, R., and H. C. Muller-Landau (2000), Spatial patterns of seed dispersal, their determinants and consequences for recruitment, *Trends Ecol. Evol.*, *15*(7), 278–285.
- Nathan, R., G. G. Katul, H. S. Horn, S. M. Thomas, R. Oren, R. Avissar, S. W. Pacala, and S. A. Levin (2002), Mechanisms of long-distance dispersal of seeds by wind, *Nature*, *418*(6896), 409–413.
- Necker, F., C. Härtel, L. Kleiser, and E. Meiburg (2002), High-resolution simulations of particle-driven gravity currents, *Int. J. Multiphase Flow*, *28*(2), 279–300.
- Ortiz, P., and P. K. Smolarkiewicz (2006), Numerical simulation of sand dune evolution in severe winds, *Int. J. Num. Meth. Fl.*, *50*(10), 1229–1246.
- Ortiz, P., and P. K. Smolarkiewicz (2009), Coupling the dynamics of boundary layers and evolutionary dunes, *Phys. Rev. E*, *79*(4), 041,307.
- Packman, A. I., and N. H. Brooks (2001), Hyporheic exchange of solutes and colloids with moving bed forms, *Water Resour. Res.*, *37*(10), 2591–2605.
- Packman, A. I., M. Salehin, and M. Zaramella (2004), Hyporheic exchange with gravel beds: basic hydrodynamic interactions and bedform-induced advective flows, *J. Hydraul. Eng.*, *130*(7), 647–656.
- Pan, Y., M. Chamecki, and S. A. Isard (2013), Dispersion of heavy particles emitted from area sources in the unstable atmospheric boundary layer, *Bound.-Layer Meteorol.*, *146*(2), 235–256.
- Pan, Y., M. Chamecki, and S. A. Isard (2014), Large-eddy simulation of turbulence and particle dispersion inside the canopy roughness sublayer, *J. Fluid Mech.*, *753*, 499–534.
- Pan, Y., M. Chamecki, S. A. Isard, and H. M. Nepf (2015), Dispersion of particles released at the leading edge of a crop canopy, *Ag. Forest Meteorol.*, *211*, 37–47.
- Perla, R. I., M. Martinelli Jr, et al. (1976), *Avalanche handbook., Agriculture Handbook, US Department of Agriculture*, 238 pp.
- Pruppacher, H. R., J. D. Klett, and P. K. Wang (1998), *Microphysics of clouds and precipitation*, Taylor & Francis, 954 pp.
- Roulund, A., B. M. Sumer, J. Fredsøe, and J. Michelsen (2005), Numerical and experimental investigation of flow and scour around a circular pile, *J. Fluid Mech.*, *534*, 351–401.
- Sarchilli, C., M. Frezzotti, P. Grigioni, L. De Silvestri, L. Agnoletto, and S. Dolci (2010), Extraordinary blowing snow transport events in East Antarctica, *Clim. Dyn.*, *34*(7-8), 1195–1206.
- Schneiderbauer, S., and A. Prokop (2011), The atmospheric snow-transport model: SnowDrift3D, *J. Glaciol.*, *57*(203), 526–542.
- Schweizer, J., J. Bruce Jamieson, and M. Schneebeli (2003), Snow avalanche formation, *Rev. Geophys.*, *41*(4).
- Shao, Y., and A. Li (1999), Numerical modelling of saltation in the atmospheric surface layer, *Bound.-Layer Meteorol.*, *91*(2), 199–225.
- Shao, Y., M. Raupach, and P. Findlater (1993), Effect of saltation bombardment on the entrainment of dust by wind, *J. Geophys. Res.*, *98*(D7), 12,719–12,726.
- Shao, Y., K.-H. Wyrwoll, A. Chappell, J. Huang, Z. Lin, G. H. McTainsh, M. Mikami, T. Y. Tanaka, X. Wang, and S. Yoon (2011), Dust cycle: An emerging core theme in earth system science, *Aeolian Res.*, *2*(4), 181–204.
- Shotorban, B., and S. Balachandar (2007), An Eulerian model for large-eddy simulation of concentration of particles with small Stokes numbers, *Phys. Fluids*, *19*(11), 118,107.
- Sleijpen, G. L., and D. R. Fokkema (1993), BiCGstab(l) for linear equations involving unsymmetric matrices with complex spectrum, *Electron. Trans. Numer. Anal.*, *1*(11), 2000.
- Smagorinsky, J. (1963), General circulation experiments with the primitive equations, *Mon. Weather Rev.*, *91*(3), 99–164.
- Sokolik, I., D. Winker, G. Bergametti, D. Gillette, G. Carmichael, Y. Kaufman, L. Gomes, L. Schuetz, and J. Penner (2001), Introduction to special section: Outstanding problems in quantifying the radiative impacts of mineral dust, *J. Geophys. Res.*, *106*(D16), 18,015–18,027.
- Sotiropoulos, F., and A. Khosronejad (2016), Sand waves in environmental flows: Insights gained by coupling large-eddy simulation with morphodynamics, *Phys. Fluids*, *28*(2), 021,301.
- Squires, K. D., and J. K. Eaton (1991), Preferential concentration of particles by turbulence, *Phys. Fluids A*, *3*(5), 1169–1178.

- Stoll, R., and F. Porté-Agel (2006), Dynamic subgrid-scale models for momentum and scalar fluxes in large-eddy simulations of neutrally stratified atmospheric boundary layers over heterogeneous terrain, *Water Resour. Res.*, *42*(1).
- Udaykumar, H., W. Shyy, and M. Rao (1996), Elafint: a mixed Eulerian–Lagrangian method for fluid flows with complex and moving boundaries, *Int. J. Num. Meth. Fluids*, *22*(8), 691–712.
- Udaykumar, H., R. Mittal, P. Rampunggoon, and A. Khanna (2001), A sharp interface Cartesian grid method for simulating flows with complex moving boundaries, *J. Comp. Phys.*, *174*, 345–380.
- Van der Vorst, H. A. (2003), *Iterative Krylov methods for large linear systems*, vol. 13, Cambridge University Press, 236 pp.
- Venditti, J. G., M. A. Church, and S. J. Bennett (2005), Bed form initiation from a flat sand bed, *J. Geophys. Res.*, *110*(F1).
- Vinkovic, I., C. Aguirre, M. Ayrault, and S. Simoëns (2006), Large-eddy simulation of the dispersion of solid particles in a turbulent boundary layer, *Bound.-Layer Meteorol.*, *121*(2), 283–311.
- Vogel, S., M. Eckerstorfer, and H. Christiansen (2012), Cornice dynamics and meteorological control at Gruvefjellet, Central Svalbard, *Cryosphere*, *6*(1), 157–171.
- Walker, D., J. C. Halfpenny, M. D. Walker, and C. A. Wessman (1993), Long-term studies of snow-vegetation interactions, *BioScience*, pp. 287–301.
- Wang, L.-P., and M. R. Maxey (1993), Settling velocity and concentration distribution of heavy particles in homogeneous isotropic turbulence, *J. Fluid Mech.*, *256*, 27–68.
- Wu, W., W. Rodi, and T. Wenka (2000), 3D numerical modeling of flow and sediment transport in open channels, *J. Hydraul. Eng.*, *126*(1), 4–15.
- Yang, D., B. Chen, M. Chamecki, and C. Meneveau (2015), Oil plumes and dispersion in Langmuir, upper-ocean turbulence: Large-eddy simulations and K-profile parameterization, *J. Geophys. Res.*, *120*(7), 4729–4759.
- Yang, D., B. Chen, S. A. Socolofsky, M. Chamecki, and C. Meneveau (2016), Large-eddy simulation and parameterization of buoyant plume dynamics in stratified flow, *J. Fluid Mech.*, *794*, 798–833.
- Ye, T., R. Mittal, H. Udaykumar, and W. Shyy (1999), An accurate Cartesian grid method for viscous incompressible flows with complex immersed boundaries, *J. Comp. Phys.*, *156*(2), 209–240.
- Zedler, E. A., and R. L. Street (2001), Large-eddy simulation of sediment transport: currents over ripples, *J. Hydraul. Eng.*, *127*(6), 444–452.
- Zwaafink, C. G., M. Diebold, S. Horender, J. Overney, G. Lieberherr, M. Parlange, and M. Lehning (2014), Modelling small-scale drifting snow with a Lagrangian stochastic model based on large-eddy simulations, *Bound.-Layer Meteorol.*, *153*(1), 117–139.

Corresponding author: S. T. Salesky, School of Meteorology, University of Oklahoma, 120 David L. Boren Blvd. #5900, Norman, OK 72073. (salesky@ou.edu)